Ceramics International 51 (2025) 49517–49533

Contents lists available at ScienceDirect

Ceramics International

journal homepage: www.elsevier.com/locate/ceramint

# Fabrication of novel $Li^{+}$ and $Sm^{3+}$ doped $CeO_2$@PVP orangish-red luminescent hybrid nanofiber for investigation of structural, optical and antibacterial activity: Unusual electronic transition modification by $Li^{+}$ doping

Kubra Nur Kavas [a], Elif Gungor [b], Yasemin Acar [b], Fatma Unal [c,d], Ozay Eroglu [e], Mehmet Emin Diken [f], Serap Dogan [f], Mustafa Burak Coban [b,*]

[a] Department of Physics, Graduate School of Natural and Applied Sciences, Balikesir University, Balikesir, Turkiye
[b] Department of Physics, Faculty of Science and Letter, Balikesir University, Balikesir, Turkiye
[c] Department of Biomedical Engineering, Faculty of Engineering and Natural Sciences, Samsun University, Samsun, Turkiye
[d] Vocational School of Technical Sciences, Samsun University, Samsun, Turkiye
[e] Department of Energy, Graduate School of Natural and Applied Sciences, Mugla Sıtkı Kocman University, Mugla, Turkiye
[f] Department of Molecular Biology and Genetic, Faculty of Science and Letter, Balikesir University, Balikesir, Turkiye

ARTICLE INFO

Handling Editor: Dr P. Vincenzini

*Keywords:*
$Li^{+}$-$Sm^{3+}$:$CeO_2$@PVP
Electropinning
Orangish-red luminescent
PL
Antibacterial effect

ABSTRACT

$Sm^{3+}$-doped and $Sm^{3+}/Li^{+}$ co-doped $CeO_2$ nanofibers were synthesized via a co-precipitation-assisted electrospining method. $Li^{+}$ co-doping led to an improvement in both crystallinity and luminescence efficiency. XRD with W-H and Scherer showed single-phase $CeO_2$ with lattice modifications due to doping. In $Sm^{3+}$ and $Li^{+}$ doped NFs, it is observed that the aggregation size gradually increases and becomes localizes at different regions within the NFs, favoring the formation of a random aggregation distribution. The porous nature of the fibers with large gaps between NFs makes them potential candidates for moisture sensors. PL measurements revealed an intense yellow emission at 574 nm ($^4G_{5/2} \rightarrow {}^6H_{5/2}$) instead of the hypersensitive electric dipole transition at 669 nm ($^4G_{5/2} \rightarrow {}^6H_{9/2}$) in $Sm^{3+}$-doped NFs, supporting the magnetic dipole transitions of the $CeO_2$ host and revealing that $Sm^{3+}$ ions are located in a position of high symmetry with an inversion center in the local medium, which underlines the efficient luminescence mechanisms within the $CeO_2$ host. The calculated critical distance ($R_c$ = 19.66 Å) indicated that energy migration occurs predominantly through electric multipolar interactions facilitated by the structural features of the NF matrix. When cryogenic temperatures were reached for $CeO_2$:0.02$Sm^{3+}$0.05$Li^{+}$@PVP NF, the partially magnetic and partially electric dipole character attributed to the $^4G_{5/2} \rightarrow {}^6H_{7/2}$ transition became dominant, as $Li^{+}$ doping reduced the possibility of $Sm^{3+}$ ions occupying asymmetric sites in the $CeO_2$ lattice. The analyzed correlated color temperature (CCT) values suggest that the prepared $Sm^{3+}$-doped nanofibers are promising "cold" candidates with commercial potential for solid-state applications, exhibiting a high color purity of 72.7 %. Moreover, under the tested conditions, $CeO_2$ and $Sm^{3+}$ ion-doped nanofibers exhibited no measurable antibacterial activity. However, $Li^{+}$ incorporation significantly enhanced antimicrobial performance without inducing cytotoxic effects, thereby supporting cell viability.

## 1. Introduction

In recent years, the production of multifunctional materials has made a great impact in scientific environments. In this context, one of the most effective approaches to combining the properties of both nanoparticles (NPs) and polymer matrices is the fabricaiton of nanofibers via electrospinning. Electrospinning is considered one of the best top-down methods for the formation of nanostructured materials [1,2]. Nanofibres (NFs) are typically fabricated from polymers; however, alternative materials such as colloidal particles, nanocomposites, micromolecules and organic polymers can also be employed. Electrospinning uses an electric charge to create NFs from a droplet of liquid. Electrospun NFs exhibit

* Corresponding author.
*E-mail address:* burakcoban@balikesir.edu.tr (M.B. Coban).

https://doi.org/10.1016/j.ceramint.2025.08.192
Received 8 June 2025; Received in revised form 27 July 2025; Accepted 13 August 2025
Available online 13 August 2025

exceptional mechanical strength, high porosity, high surface-to-volume ratio, and nanoscale effects [3,4]. Membrane separation, drug delivery, protective clothing, tissue engineering, wound dressings, filtration and electronics are just a few of the proposed applications [5]. In polymers, the emphasis is placed on improved properties and environmental sustainability. Polyethylene glycol (PEG), poly(vinyl pyrrolidone) (PVP) and poly(vinyl alcohol) (PVA) are versatile polymers. These polymers are easy to process, biodegradable, non-toxic and useful for various medical and engineering applications [6,7]. PVP contains functional groups that form interchain hydrogen bonds, making it a good capping and binding agent in complex material composites [8]. Its amorphous structure, when combined with semiconducting crystalline nanostructures, minimizes the scattering coefficient, thus rendering it an ideal polymer for a wide range of composite material applications. Another notable feature is its high solubility in water, which prevents phase separation and further enhances its suitability as a preferred polymer in advanced material systems [9–11].

Rare-earth oxides have garnered significant scholarly interest due to their multifaceted applications, including but not limited to oxygen sensors, photocatalysts, fuel cells, and solar cells [12–15]. Among these compounds, cerium oxide (Ceria) possesses distinctive physical and chemical characteristics that render it exceptionally valuable. Ceria exhibits a cubic crystalline structure and is categorized within the fluorite family, possessing a space group of *Fm-3m*; it predominantly absorbs light photons from the near-ultraviolet spectrum while capturing a limited range of visible photons. Consequently, ceria can harness a substantial fraction of solar radiation, and materials containing $CeO_2$ have been utilized as proficient oxidizing catalysts, attributed to their unique redox capabilities and oxygen storage proficiency [16,17]. Furthermore, cerium oxide exhibits a substantial quantity of surface oxygen vacancies [18]. These oxygen vacancies present on the $CeO_2$ surface possess the capacity to both store and release oxygen, in addition to functioning as catalytic sites [19,20]. The concentration of oxygen vacancies on the $CeO_2$ surface can be augmented through the reduction of pure $CeO_2$ in a hydrogen-rich environment [21,22] or by the introduction of suitable dopant elements [23,24]. Notwithstanding the enhancement of oxygen vacancies through doping, the primary prerequisite is carefully selecting dopants that possess appropriate ionic radii and concentrations.

The alkaline $Li^+$ ion, assigned as a charge-compensating agent, can significantly improve the luminescence potential in suitable substrates. Lithium ions co-doped into the $CeO_2$:$Sm^{3+}$ NP lattice enhance luminescence by exploiting the lithium ions' flux nature. The ionic radius of $Li^+$ ions is small, so they can merge into the $CeO_2$ lattice to create oxygen vacancies for energy transfer. Furthermore, these monovalent cations can affect the crystal field environment by acting as charge carriers, generally leading to improved crystallinity, reduced concentration quenching, and increased quantum yield [25–27]. Recent literature suggests that the luminescence behavior of rare earth ions and the charge compensatory role of $Li^+$ are not limited to a specific host lattice, but are also observed in structurally similar matrices. For instance, Guo et al. [28] recently demonstrated that $Li^+$ co-doping in $Er^{3+}$-doped $CeO_2$ enhances intense green and red upconversion luminescence and structural uniformity by modifying the local lattice field and local symmetry and by suppressing non-radiative losses. Furthermore, they reported that the visible spectral transmittance of $CeO_2$:$Er^{3+}$, $Li^+$ ceramics increased with the incorporation of $Li^+$ ions. Youl Jung et al. [29] reported that the co-doping of monovalent alkali ions ($Li^+$, $Na^+$, and $K^+$) in $Eu^{3+}$-doped $CeO_2$ significantly enhances the emission intensity of $CeO_2$:$Eu^{3+}$ nanophosphors through improved crystallinity and charge balancing, resulting in intense red emission visible to the naked eye under 365 nm LED light. Altowyan et al. [30] recently showed that the co-doping of $Eu^{3+}$ and $Li^+$ in $ZrO_2$ nanophosphors improved charge compensation and enhanced intense red and far-red emissions by altering local symmetry. They proposed that Li $^+$ doping not only significantly increases emission intensity by stabilizing the tetragonal phase and forming oxygen vacancies but also limits the concentration quenching process. These findings support the notion that understanding $RE^{3+}$and $Li^+$ co-doping mechanisms in rare earth oxide—and metal oxide— host lattices can provide more comprehensive insights into luminescent behavior across material systems. To the best of our knowledge, no other study has reported the photoluminescence properties of $CeO_2$@PVP NFs doped with $Sm^{3+}$ ions and alkali metal ions ($Li^+$) acting as charge compensators. In this sense, this research investigates orange-emitting $CeO_2$@PVP doped with samarium ($Sm^{3+}$) ions and co-doped with $Li^+$, synthesized by an electrospinning route. The phase structure, morphology, composition and biological properties of the $CeO_2$:$Sm^{3+}$, $Li^+$@PVP NFs were investigated. The addition of alkali co-dopants improved the NFs performance. The team also investigated temperature-dependent photoluminescence, color coordinates and photometric properties. These results reveal a new type of orange cerium oxide NF with potential for use in UV-excitable NF-converted white LEDs.

## 2. Experimental details

### 2.1. Materials and instrumentation

The materials used in this study were cerium nitrate hexahydrate ($Ce(NO_3)_3{\cdot}6H_2O$, Sigma-Aldrich Co.), samarium nitrate hexahydrate ($Sm(NO_3)_3{\cdot}6H_2O$, 99.9 %), lithium nitrate ($LiNO_3$, 99.99 %), polyvinylpyrrolidone (PVP, Mw ~ 1300,000 by LS, in powder form) and sodium hydroxide (NaOH, reagent grade, ≥98 %, pellets), all purchased from Sigma-Aldrich Co. All chemicals were of analytical grade and used without further purification. Fourier-transform infrared (FT-IR) spectroscopy (Thermo Scientific Nicolet iS50) was employed to confirm functional groups and binding environments in the range of 4000–600 $cm^{-1}$ at room temperature. Scanning electron microscopy (SEM) images were recorded using a FEI Quanta 650 FEG. The average diameter and their distribution of the composite NFs were determined from SEM images using Image J software. Photoluminescence (PL) spectra were measured with an ANDOR SR500i-BL luminescence spectrometer equipped with a triple grating and detected by Intensified Charge Coupled Device (ICCD) camera as a detector for the visible region. A frequency tripled Nd:YLFQ switched pulse laser at 349 nm was used for the excitation source. X-ray diffraction (XRD) was used to examine phase composition and crystallinity, with a Malvern Panalytical Empyrean diffractometer ($CuK_\alpha$, $\lambda = 1.5406$ Å) being used for the analysis. The data were collected over a 2θ range of 20°–80° with a step size of 0.02°.

### 2.2. Synthesis of $CeO_2$:$xSm^{3+}$,$yLi^+$ NPs

The synthesis of undoped $CeO_2$ NPs and their doped counterparts ($CeO_2$:$Sm^{3+}$ and $CeO_2$:$Sm^{3+}$:$Li^+$) followed a systematic approach. The precipitation method was employed to fabricate undoped $CeO_2$ nanoparticles using cerium nitrate hexahydrate as the starting material. This was followed by the preparation of a 0.1 M solution of $Ce(NO_3)_3{\cdot}6H_2O$ in 100 mL of distilled water (DI), and a separate 0.2 M solution of NaOH in another 50 mL of distilled water. The 0.2 M sodium hydroxide solution was added to the cerium nitrate hexahydrate solution until a final pH of 7 was reached, and the mixture was stirred for 4 h at 80 °C. The resulting suspension underwent purification through successive washes with DI and ethanol. After centrifugation at 4000 rpm for 10 min, the obtained material was dried in an oven at 80 °C overnight. Subsequently, the dried material was finely ground using an agate mortar and subjected to a 3 h calcination process at 600 °C (Scheme 1a). A similar methodology was applied to the synthesis of $CeO_2$:$Sm^{3+}$ NPs. In this case, the 0.1 M solution of $Ce(NO_3)_3{\cdot}6H_2O$ was prepared by adding $Sm^{3+}$ ions in varying weight percentages (x = 1, 2, 3, 5, and 7) from the nitrate salt of $Sm^{3+}$ ($Sm(NO_3)_3{\cdot}6H_2O$). The next steps were consistent with those used for undoped $CeO_2$ NPs. A parallel approach was taken to create $CeO_2$:

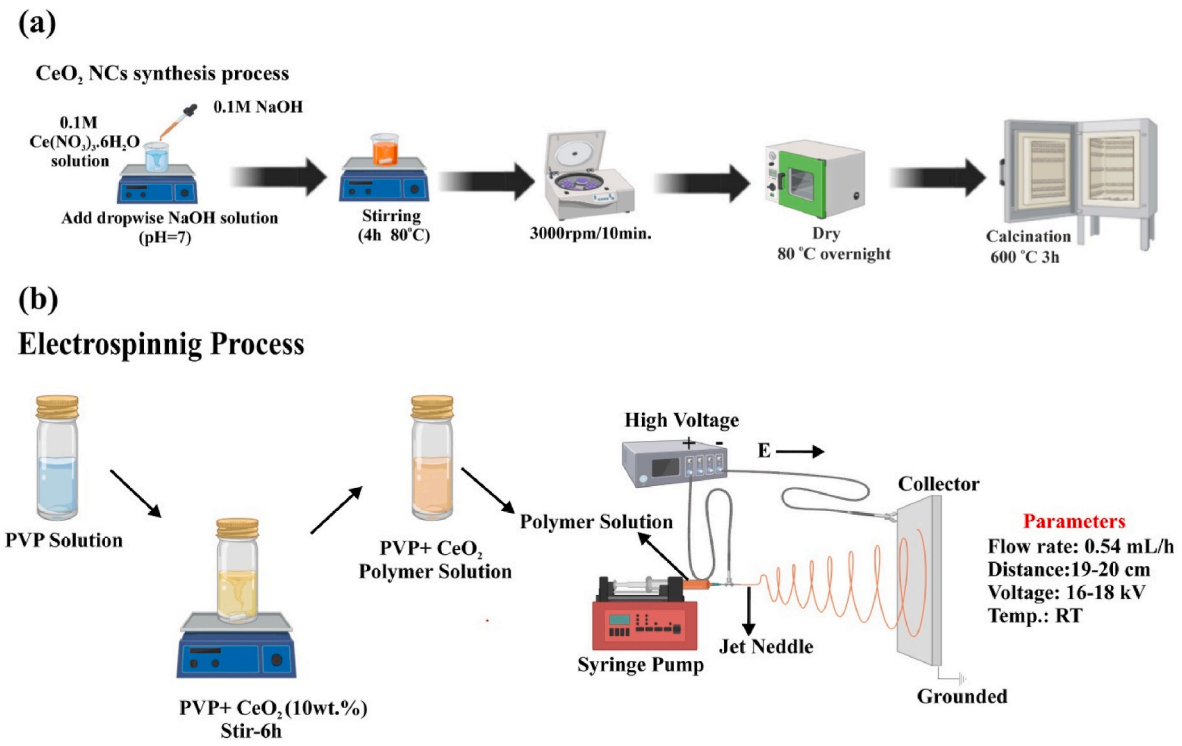


**Scheme 1.** Synthesis route of **(a)** $CeO_2$ NCs and **(b)** electrospinning process of the $CeO_2$@PVP NFs.

$Sm^{3+}$,$Li^+$ dual-doped NPs. The 0.1 M solution of $Ce(NO_3)_3{\cdot}6H_2O$ was prepared with 1 wt % $Sm^{3+}$ and varying weight percentages (y = 1, 2, 3, 5, and 7) of $Li^+$ ions from the nitrate salt of $Li^+$ ($LiNO_3$).

### 2.3. Preparation of spinning solutions

Typically, PVP (15 % w/v) is used as the matrix material. 15 g of PVP is dissolved in 100 mL of EtOH and stirred for 24 h at room temperature. Then, similar proportions of $CeO_2$, $CeO_2$:$x$$Sm^{3+}$, and $CeO_2$:0.02$Sm^{3+}$, $y$$Li^+$ (x and y = 1, 2, 3, 5, and 7 wt%) NPs are added and stirred for 12 h at room temperature for homogenization and transparency. Finally, sonication is applied for 30 min to remove bubbles.

### 2.4. Preparation of composite NFs

Electrospinning was performed in a horizontal alignment using a 16–18 kV DC high-voltage generator and a laboratory spinning unit (SPINGENIX SG-1). A 10 mL plastic injector with a non-rust steel needle (0.8 mm inner diameter) was used to eject the spinning solution. The needle tip was 19–20 cm from the collector. The fluid supply rate was 0.54 mL/h, and the NFs were collected on aluminium foil. The composite NFs were dried in a vacuum-drying oven at 40 °C for 12 h (Scheme 1b).

### 2.5. Antioxidant properties of NFs

The antioxidative potential of the samples was assessed using the DPPH (2,2-Diphenyl-1-picrylhydrazyl) and ABTS (2,2′-Azino-bis[3-ethylbenzothiazoline-6-sulfonic acid]) radicals utilizing a UV–Visible spectrophotometer (PerkinElmer Lambda-35, USA). The DPPH radical was prepared at a concentration of 0.6 mM by dissolving the compound in methanol (MeOH) within a dark flask. The $ABTS^+$ radical solution was synthesized by combining equal volumes of 7 mM ABTS salt and 2.4 mM ammonium persulfate, subsequently incubated in darkness overnight. Thereafter, the solutions were diluted with MeOH until achieving an absorbance of 1.50 ± 0.01 at a wavelength of 517 nm and 734 nm. Each sample was accurately weighed to approximately 10 mg and subsequently introduced into 1 ml of the radical solution (DPPH and $ABTS^+$). Following a vortexing period of 30 s, the absorbance was quantified at 517 nm for DPPH and 734 nm for $ABTS^+$ radicals, respectively. Each measurement was performed in triplicate for all samples. Utilizing the acquired data, the antioxidant activity of the samples was calculated in accordance with the following Equation (1) [31]:

$$I(\%) = \frac{Acontrol - Asample}{Acontrol}\ x\ 100 \quad (1)$$

where I (%) is percentage of inhibition, $A_{control}$ is absorbance of DPPH or ABTS in methanolic solution, and Asample is absorbance of DPPH or ABTS solution.

### 2.6. Biocompatibility analysis of sample

The principal objective of the biocompatibility assessment was to evaluate the extent of hemolysis in cells upon their interaction with the experimental samples. Consequently, a volume of 2 mL of human blood was collected in citrate tubes to inhibit coagulation. The anticoagulated blood was then diluted at a ratio of 1:5 with a saline solution (9 mM NaCl). For the positive control, 0.2 mL of the diluted blood was combined with 0.5 mL of 0.01 M HCl and incubated at a temperature of 37 °C for a duration of 2 h followed, by dilution to a final volume of 10 mL. In a comparable manner, for the negative control, 0.2 mL of the diluted blood was further diluted to 10 mL with the addition of the saline solution and incubated at 37 °C for 2 h. The mixture, consisting of 0.2 mL of diluted blood in a centrifuge tube combined with 9.8 mL of saline solution, was incubated at 37 °C for 15 min to achieve thermal equilibrium. Samples weighing 10 mg were subsequently introduced into centrifuge tubes containing the blood-saline mixture and incubated for a period of 2 h at 37 °C. Following the incubation period, all sample solutions underwent centrifugation at 5000 rpm for 10 min, and upon careful removal of the supernatant, the supernatant designated for spectrophotometric analysis was transferred to a 96-well plate. The optical densities of the incubated sample solutions were determined

spectrophotometrically at a wavelength of 545 nm using a Thermo Scientific Multiskan-GO UV/Visible spectrophotometer. The percentage of hemolysis was calculated using the following equation [32]:

$$Hemolysis\ (\%) = \frac{(ODtest - ODnegative)}{ODpositive - ODnegative)}\ x\ 100 \quad (2)$$

where ODtest denotes the optical density of the sample solution; ODpositive represents the optical density of the positive control; and ODnegative refers to the optical density of the negative control. When the percentage of hemolysis is at or below 5 %, the sample is classified as hemocompatible. Conversely, if the hemolysis percentage reaches 10 % or less, it is categorized as biocompatible.

### 2.7. Antibacterial efficiency of sample

The antibacterial characteristics of the samples were evaluated against *Escherichia coli* and *Staphylococcus aureus* employing the agar diffusion methodology. Bacterial cultures were prepared to a concentration of close to $10^5$ CFU/mL in nutrient broth. Subsequently, a well of 6 mm in diameter was created on the Mueller Hinton agar, which serves to assess the inhibition zone. Thereafter, 10 mg of each powdered sample was introduced into the prepared well. The inoculated agar plates were subjected to incubation at a temperature of 37 °C for a duration of 24 h under aerobic conditions. The measurement of the zone of inhibition was conducted utilizing the millimeter scale. The presence of a zone of inhibition surrounding the wells indicates the antibacterial efficacy of the samples.

## 3. Results and discussion

### 3.1. XRD analysis

The diffraction pattern of the $CeO_2$:$x$Sm$^{3+}$ and $CeO_2$:0.02Sm$^{3+}$:$y$Li$^+$ luminescent samples is presented in Fig. 1. All of the observed diffraction bands were aligned with the joint committee on powder diffraction

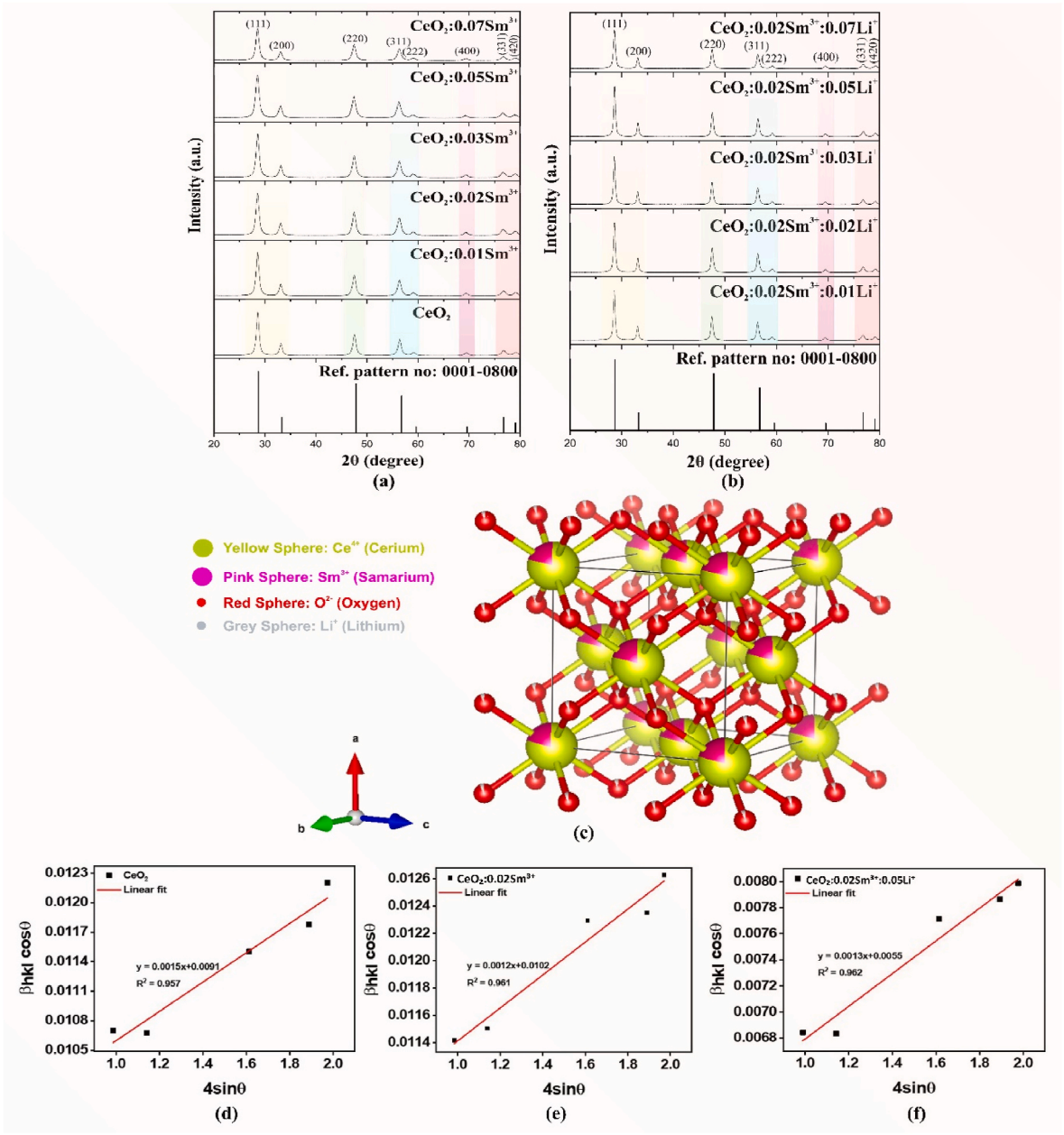


**Fig. 1.** XRD patterns and Williamson–Hall plots of $CeO_2$, $CeO_2$:0.02Sm$^{3+}$ and $CeO_2$:0.02Sm$^{3+}$,0.05Li$^+$ NPs.

standards (JCPDS) file no. 001–0800. No additional peaks related to any impurity or secondary phase was detected in the observed XRD pattern, thus reflecting the lack of influence of $Sm^{3+}$ and $Li^{+}$ ions on the crystal structure of $CeO_2$ host matrix. The sharp and distinct X-ray lines indicate high crystallinity and successful synthesis of $CeO_2$ NPs. Thus, $CeO_2$, $Sm^{3+}$ doped $CeO_2$ and $Li^{+}$ doped $CeO_2$:0.02$Sm^{3+}$ synthesized NPs possess a cubic structure with space group *Fm-3m* (225).

The crystallite size (CS) values were determined using various models, including the Debye-Scherrer (D-S) and Williamson-Hall (W-H) methods, based on the X-ray diffraction (XRD) data, while the dislocation density (DD) values were calculated using the Williamson-Smallman (W-S) method [33]. The values of crystallite size (CS), lattice parameters (LP), volume of unit cell (VC), and dislocation density (DD) for the samples are presented in Table 1.

X-ray diffraction (XRD) is a widely used technique for determining the average crystallite size of powders (see Table 2). Initially, the crystallite size was calculated using the D-S method, as given in Equation (3), with the following formula [33,34]:

$$D = \frac{k\lambda}{\beta \cos\theta} \tag{3}$$

where $\beta$ represents the XRD diffraction peak broadening, $\lambda$ is the X-ray wavelength, θ is the Bragg angle, and $k$ and $D$ denote the shape factor and crystallite size, respectively.

The crystallite size (CS) and lattice strain (LS) values were obtained using W-H analysis, incorporating the Uniform Deformation Model (UDM). The broadening of XRD peaks is influenced by the CS, LS, and instrumental broadening. To eliminate the effect of instrumental broadening, it was first corrected using the XRD data of a standard silica sample, as outlined in Equation (4) [33,34].

$$\beta_{hkl} = \left[(\beta_{hkl})^2_{(measured)} - \beta^2_{(instrumental)}\right]^{1/2} \tag{4}$$

The strain induced by crystal defects and distortions was calculated using the following formula:

$$\varepsilon = \frac{\beta_{hkl}}{4 \tan\theta} \tag{5}$$

By combining Equation (3) with Equation (5), the following expression is derived [33,34].

$$\beta_{hkl} \cos\theta = \frac{k\lambda}{D} + (4\varepsilon \sin\theta) \tag{6}$$

Where $\beta_{hkl}$ represents the corrected XRD diffraction peak broadening, $\lambda$ is the X-ray wavelength, $k$ is the shape factor, $\theta$ is the Bragg angle, $D$ is the crystallite size, and $\varepsilon$ is the lattice strain. Based on the SEM images, which indicated that the particles had a nearly round morphology, a value of $k = 0.89$ was used. The W-H analysis integrated with the UDM was performed by plotting ($\beta_{hkl} \cos\theta$) against ($4 \sin\theta$), as shown in Fig. 1. The CS and LS were determined from the *y*-intercept and the slope of the linear fit, respectively. The Williamson-Hall (W-H) plots for the $CeO_2$, $CeO_2$:0.02$Sm^{3+}$, and $CeO_2$:0.02$Sm^{3+}$:0.05Li samples are presented in Fig. 1. The W-H plots for the remaining samples are provided in the Supplementary Information.

**Table 2**
$E_g$ values depending on the concentration of undoped, $Sm^{3+}$ and $Li^{+}$ co-dopant in $CeO_2$@PVP NFs.

| Compositions | The band gap (eV) | References |
|---|---|---|
| $CeO_2$@PVP | 3.63 | This work |
| CeO2:0.01$Sm^{3+}$@PVP | 3.60 | This work |
| $CeO_2$:0.02$Sm^{3+}$@PVP | 3.45 | This work |
| $CeO_2$:0.03$Sm^{3+}$@PVP | 3.30 | This work |
| $CeO_2$:0.05$Sm^{3+}$@PVP | 3.22 | This work |
| $CeO_2$:0.07$Sm^{3+}$@PVP | 3.26 | This work |
| $CeO_2$:0.02$Sm^{3+}$:0.01$Li^{+}$@PVP | 3.60 | This work |
| $CeO_2$:0.02$Sm^{3+}$:0.02$Li^{+}$@PVP | 3.62 | This work |
| $CeO_2$:0.02$Sm^{3+}$:0.03$Li^{+}$@PVP | 3.67 | This work |
| $CeO_2$:0.02$Sm^{3+}$:0.05$Li^{+}$@PVP | 3.68 | This work |
| $CeO_2$:0.02$Sm^{3+}$:0.07$Li^{+}$@PVP | 3.69 | This work |
| $CeO_2$, $CeO_2$:Nd and $CeO_2$:Gd | 3.46,3.39 and 3.30 | [48] |
| $CeO_2$ | 3.35 | [49] |
| $CeO_2$ | 3.06 | [50] |
| $CeO_2$ | 3.17 | [51] |

Dislocation density, which quantifies crystal defects that influence the rigidity, stiffness, strength, and ductility of materials, plays a crucial role in material properties. Therefore, it is essential to control these crystal imperfections. The dislocation density (DD) is determined using the Williamson-Smallman (W-S) method (Equation (7)) [33].

$$\delta = \frac{1}{D^2} \tag{7}$$

Where $D$ represents the crystallite size and δ denotes the dislocation density, respectively.

The crystallite size (CS), lattice parameter (LP), and dislocation density (DD) values exhibit significant variations depending on the dopant type and concentration. For undoped $CeO_2$, the CS values calculated using the Debye-Scherrer (D-S) and Williamson-Hall (W-H) methods were 12.77 nm and 15.07 nm, respectively. The LP for this sample was 5.412 Å, and the DD was calculated as $4.403 \times 10^{-3}$ $nm^{-2}$. With increasing $Sm^{3+}$ doping, the CS values decreased, reaching 10.98 nm (D-S) and 13.57 nm (W-H) for $CeO_2$:0.02$Sm^{3+}$, indicating the impact of dopant-induced strain and defects. This trend was reflected in the DD values, which rose to $11.341 \times 10^{-3}$ $nm^{-2}$ for $CeO_2$:0.05$Sm^{3+}$, highlighting the increased defect density associated with higher $Sm^{3+}$ concentrations.

In contrast, co-doping with $Li^{+}$ in $Sm^{3+}$-doped samples significantly increased the CS values, reaching up to 19.53 nm (D-S) and 24.93 nm (W-H) for $CeO_2$:0.01$Sm^{3+}$:0.05$Li^{+}$. These findings suggest that $Li^{+}$/$Sm^{3+}$ co-doping mitigates strain effects and promotes particle growth. Furthermore, the DD values for $Li^{+}$/$Sm^{3+}$ co-doped samples were markedly lower, with $CeO_2$:0.01$Sm^{3+}$:0.05$Li^{+}$ exhibiting a DD of only

**Table 1**
Geometric parameters of undoped $CeO_2$ and $Li^{+}$/$Sm^{3+}$ doped $CeO_2$ NPs obtained from PXRD.

| Sample code | (111) plane | | | CS (*D*/nm) | | DD (δ/$nm^{-2}$,$10^{-3}$) | LS (ε) |
|---|---|---|---|---|---|---|---|
| | $2\theta_{hkl}$ | LP (a/Å) | VC ($V/Å^3$) | W-H | D-S | | |
| $CeO_2$ | 28.54 | 5.412 | 158.516 | 15.07 | 12.77 | 4.403 | 0.0091 |
| $CeO_2$:0.01$Sm^{3+}$ | 28.52 | 5.416 | 158.868 | 13.44 | 12.05 | 5.536 | 0.0102 |
| $CeO_2$:0.02$Sm^{3+}$ | 28.50 | 5.419 | 159.132 | 13.57 | 10.98 | 5.431 | 0.0101 |
| $CeO_2$:0.03$Sm^{3+}$ | 28.54 | 5.412 | 158.516 | 13.44 | 11.01 | 5.536 | 0.0102 |
| $CeO_2$:0.05$Sm^{3+}$ | 28.50 | 5.419 | 159.132 | 9.39 | 11.03 | 11.341 | 0.0146 |
| $CeO_2$:0.07$Sm^{3+}$ | 28.58 | 5.405 | 157.902 | 12.93 | 11.04 | 5.981 | 0.0106 |
| $CeO_2$:0.02$Sm^{3+}$:0.01Li | 28.56 | 5.408 | 158.165 | 24.48 | 19.08 | 1.669 | 0.0056 |
| $CeO_2$:0.02$Sm^{3+}$:0.02Li | 28.58 | 5.405 | 157.902 | 22.47 | 19.28 | 1.981 | 0.0061 |
| $CeO_2$:0.02$Sm^{3+}$:0.03Li | 28.58 | 5.405 | 157.902 | 24.48 | 19.13 | 1.669 | 0.0056 |
| $CeO_2$:0.02$Sm^{3+}$:0.05Li | 28.62 | 5.397 | 157.202 | 24.93 | 19.53 | 1.609 | 0.0055 |
| $CeO_2$:0.02$Sm^{3+}$:0.07Li | 28.60 | 5.401 | 157.551 | 20.16 | 17.33 | 2.460 | 0.0068 |

$1.609 \times 10^{-3}$ $nm^{-2}$. The LP values for co-doped samples ranged from 5.397 Å to 5.419 Å, with slight decreases observed at higher $Li^+$ concentrations, potentially indicating improved lattice stability.

These structural improvements in co-doped samples can be mechanistically explained by the role of $Li^+$ within the $CeO_2$ lattice. Despite its lower ionic radius and monovalent nature, $Li^+$ ions can occupy interstitial or substitutional positions, enabling charge compensation and promoting the formation of oxygen vacancies. These vacancies facilitate atomic diffusion during heat treatment, which promotes crystallite growth and reduces internal lattice strain. Furthermore, the presence of $Li^+$ contributes to the relaxation of stress and healing of structural defects, resulting in improved crystallinity and lower dislocation densities. The trends observed in crystallite size, lattice strain, and dislocation density confirm the stabilizing effect of $Li^+$ co-doping on the crystal structure.

These results demonstrate how dopant type and concentration significantly influence the structural characteristics of $CeO_2$-based materials, providing valuable insights for optimizing their properties for specific applications. Specifically, $Sm^{3+}$ doping increases crystal defects and strain, while $Li^+/Sm^{3+}$ co-doping effectively reduces these imperfections, thereby enhancing the structural properties of the materials. Furthermore, the discrepancies observed between the Debye-Scherrer (D-S) and Williamson-Hall (W-H) methods underscore the importance of accounting for lattice strain when determining crystallite size.

Furthermore, the presence of $Sm^{3+}$ ions did not lead to a significant change in peak position, confirming that dopant ions occupy one of the available cationic sites and do not alter the crystal structure. The $CeO_2$ host contains a single cation, $Ce^{4+}$, with an ionic radius of 0.97 Å. $Sm^{3+}$ ions occupy the $Ce^{4+}$ sites since the $Sm^{3+}$ ionic radius (1.079 Å) is comparable to $Ce^{4+}$ [35]. Generally speaking, an acceptable percentage difference between parent cations and dopant ions can be determined by calculating a $D_r$ value from the following relation [36]:

$$D_r = \frac{|R_m(CN) - R_d(CN)|}{R_m(CN)} \times 100\%$$

If the $D_r$ for a cation-dopant pair is less than 30 %, it is more likely to occupy that cationic site. Where $R_m(CN)$ is the radius of the cation within the host matrix and $R_d(CN)$ is the radius of the dopant ion. For the $Ce^{4+}$- $Sm^{3+}$ pair in the *Fm-3m* space group (CN = 8) $D_r = 11.23$ %, which favours substitution.

### 3.2. FTIR analysis

FTIR spectroscopy is a very useful and effective method to obtain an infrared spectrum describing how additives interact with a polymeric matrix. Fig. 2 represents the ATR-FTIR spectra of PVP, different (0, 1, 2, 3, 5 and 7) wt%. $Sm^{3+}$ doped $CeO_2$@PVP NFs and different (1, 2, 3, 5 and 7) wt%. Li $^+$ doped $0.02Sm^{3+}$:$CeO_2$@PVP NFs, where the wave number values match the peaks of the main absorbance bands of the PVP blend, shown in the wave number range 600–4000 $cm^{-1}$ and identifies the chemical bonds and functional groups in the NFs [37]. To further make the findings from the FT-IR analysis more meaningful, we performed FTIR spectroscopy of PVP-only, $CeO_2$@PVP-only, $Sm^{3+}$ doped $CeO_2$@PVP and $Li^+/Sm^{3+}$ doped $CeO_2$@PVP NFs [38]. According to Fig. 5, the infrared spectrum (FTIR) of the synthesized $CeO_2$ nanoparticles was in the range of 600–4000 $cm^{-1}$ wavenumbers, identifying chemical bonds and functional groups in the compound. As shown in Fig. 2, PVP has a large number of vibrational modes. The large broadband at 3435 $cm^{-1}$ is assigned to the O-H stretching vibration in OH– groups. The bands located at around 2946, 2867 and 1426 $cm^{-1}$ are attributed to the C–H asymmetric stretching, C–H symmetric stretching and C–H deformation, respectively. The bands at around at 1655, 1366 and 1239 $cm^{-1}$ are due to C=O stretching in primary amide, C–O stretching symmetric and C–O–C stretching asymmetric), respectively [39]. The weak absorption band at 837 $cm^{-1}$ is probably due to the bond metal-oxygen interaction [40]. Compared with pure PVP NF, when $CeO_2$ NPs were incorporated into the polymeric NF, these peaks became less strong. This is comparable to the result of the XRD study. Therefore, the possibility that $CeO_2$ NPs interact with the backbone chains of carbonyl (C=O) groups in PVP is strengthened. Moreover, the changing intensity of these peaks is a good indication of the successful physical loading of $CeO_2$ NPs onto NFs with the backbone chains via van der Waals forces.

Moreover, the observed characteristic bands are consistent in all samples, indicating that the basic structure is preserved even after $Sm^{3+}$ and Li $^+$ doping. Moreover, the $Sm^{3+}$ and Li $^+$ co-doped NFs exhibit more intense peaks overall, underlining the importance of better connectivity of the NF network and fine-tuning the host matrix for improved structural order and connectivity characteristics due to the combined effects of $Sm^{3+}$ and $Li^+$. These small modifications, $Li^+$ co-doping, can improve the overall luminescent efficiency, a phenomenon consistent with PL analysis. It also indicates that small modifications can occur, leading to the lattice strains given in Table 1, thus showing a systematic consistency with the XRD results as well.

### 3.3. Morphological studies

The morphology of the prepared NFs was evaluated using scanning electron microscopy (SEM) and the results and elemental distribution maps of Ce, O, C, N, and Sm are shown in Fig. 3. The morphology of electrospun fibers is affected by both the physical and electrical properties of the solution and the ratios in the solution mixture [41]. As seen in the scanning electron microscopy images of the NFs shown in Fig. 3,

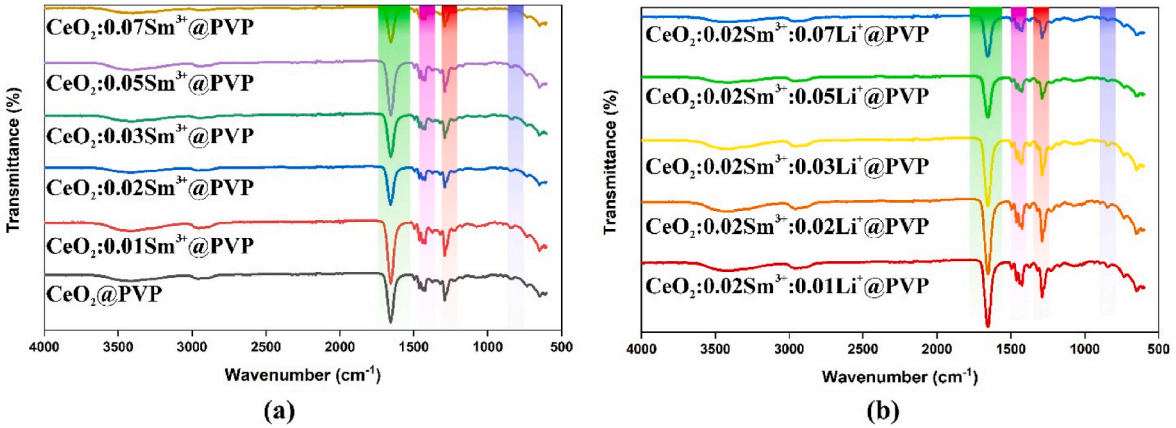


**Fig. 2.** FTIR spectra of **(a)** $CeO_2$@PVP, $CeO_2$:*x* wt.% $Sm^{3+}$@PVP (x = 1, 2, 3, 5 and 7) and **(b)** $CeO_2$:0.01$Sm^{3+}$:*y* wt.% $Li^+$@PVP (y = 1, 2, 3, 5 and 7) composite NFs in the range 4000–600 $cm^{-1}$.

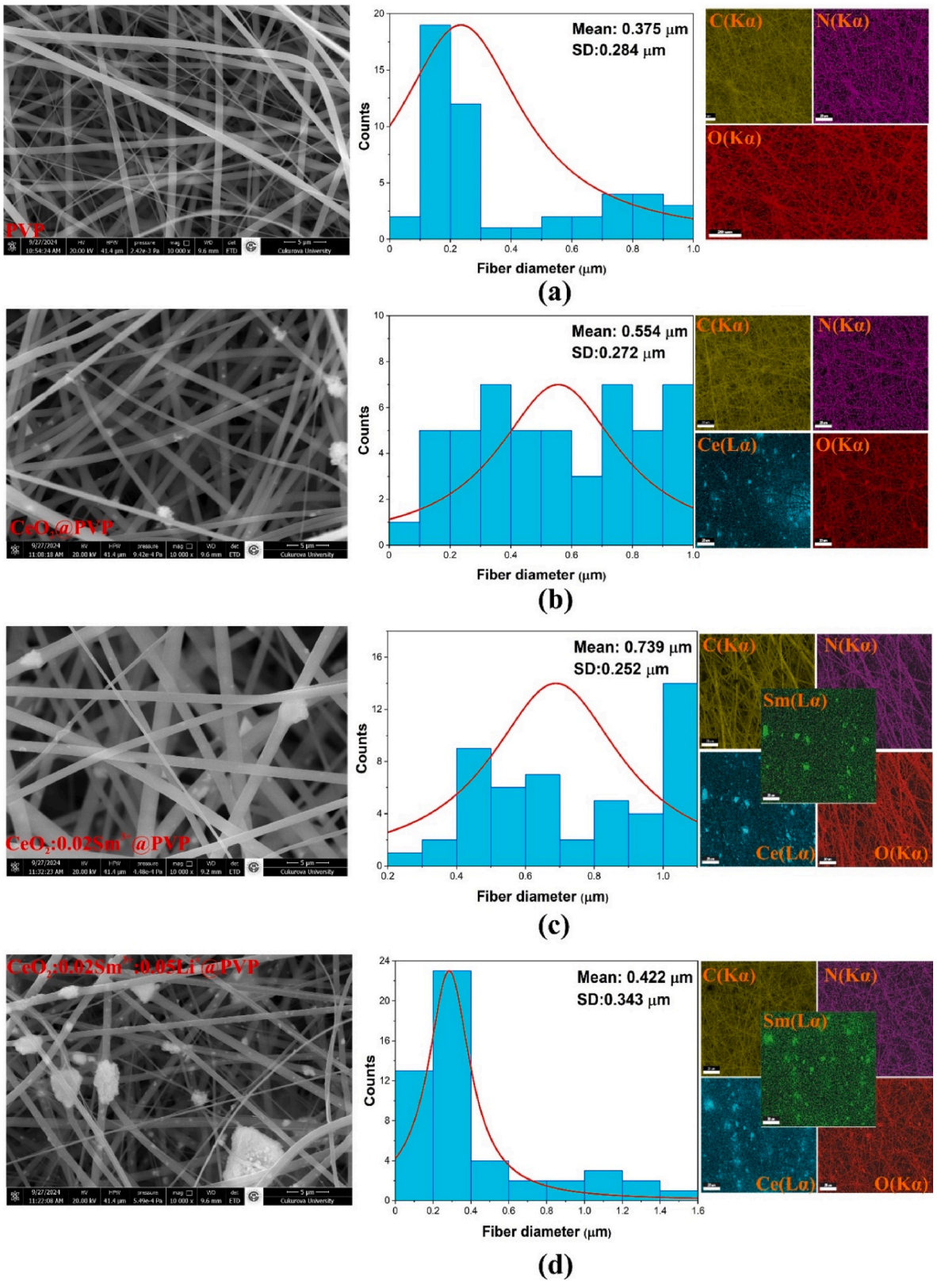


**Fig. 3.** SEM images of the synthesized PVP, $CeO_2$:@PVP, $CeO_2$:0.02$Sm^{3+}$@PVP and, $CeO_2$:0.02$Sm^{3+}$:0.05$Li^{+}$@PVP composite NFs.

NPs prepared at different concentrations were able to produce suitable NFs with all composite solutions prepared by adding the same ratio of NPs to the polymer solution. The diameters of NFs at fifty different locations were measured using Image J software, and a fiber diameter distribution plot was generated using Origin software and the average diameter values of each sample are reported in Fig. 3. The data show the average diameter and standard deviation of electrospun NFs; compared to the average fiber diameter of undoped PVP NFs, a partial increase from $CeO_2$@PVP NFs to $CeO_2$:0.02$Sm^{3+}$@PVP NFs, while $CeO_2$:0.02$Sm^{3+}$,0.05$Li^{+}$@PVP NFs exhibit a decrease promoting

formation, with average fiber diameters of 0.375, 0.554, 0.793 and 0.422 μm, respectively. The obtained findings are in agreement with the average fiber diameters of $RE^{3+}$ doped composite nanofibers in our previous reports [42,43]. Furthermore, no agglomeration was observed in the undoped $CeO_2$@PVP NFs, while fibers with different orientations and diameters can be seen in Fig. 3a. It was found that the agglomeration size in $CeO_2$:0.02$Sm^{3+}$@PVP and $CeO_2$:0.02$Sm^{3+}$,0.05$Li^+$@PVP NFs gradually increases and favours the formation of a random agglomeration distribution by settling in NFs at different locations. In $Sm^{3+}$ and $Li^+$ co-doped $CeO_2$@PVP nanofibers, the increased agglomeration with rare earth and alkali metal ion doping may be due to the rough surface of the fibers, the ionic bonds formed and the decrease in the nucleation area. The porous structure of the fibers with large voids between the final fibers will allow water molecules to penetrate easily, making them potential candidates for moisture sensing [44].

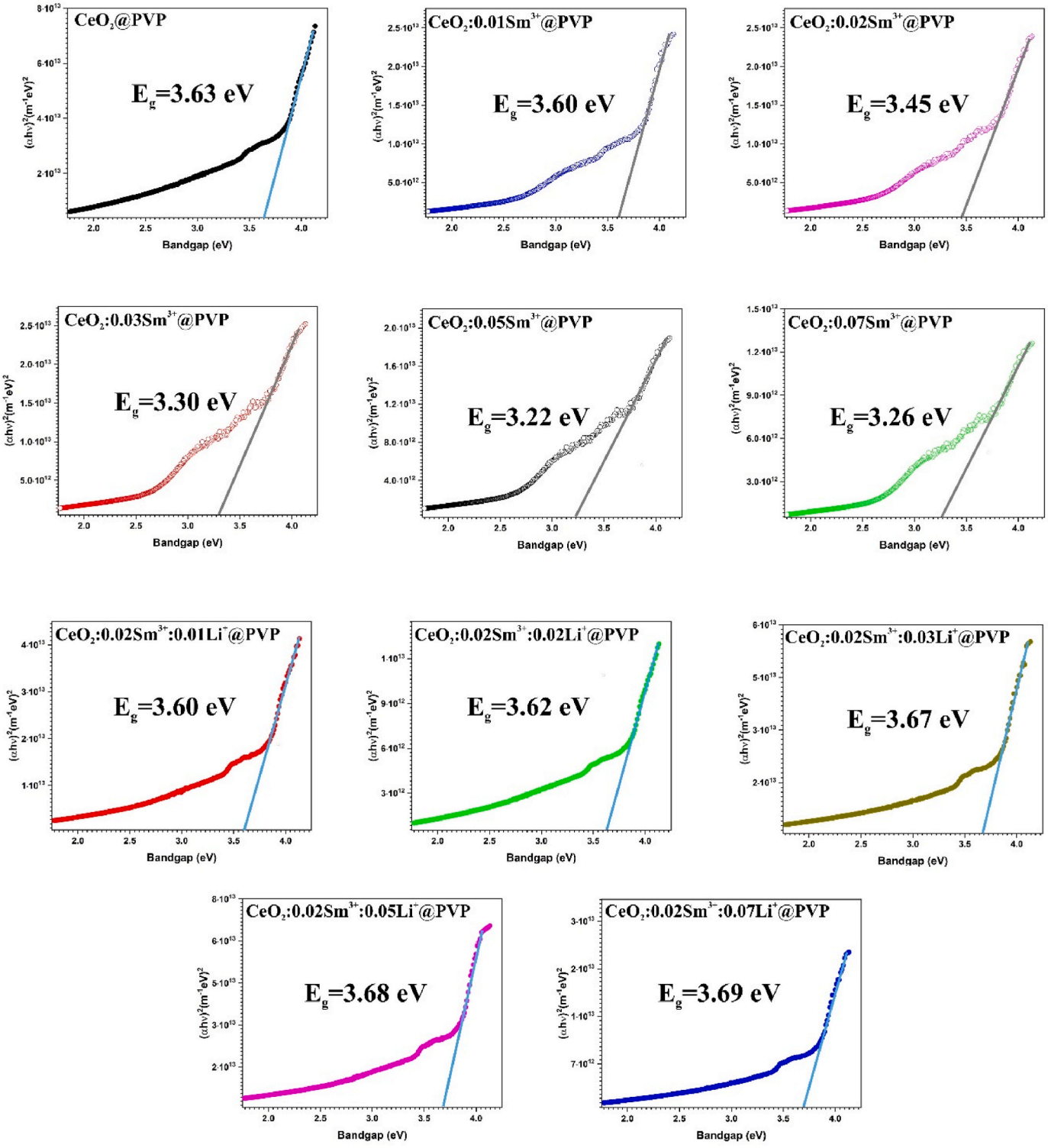


**Fig. 4.** Tauc's plot of all NFs for calculating bandgap.

### 3.4. UV–visible analysis

The optical characteristics of NF materials exemplify their interaction with electromagnetic radiation and consequently inform their prospective applications across many fields. Comprehensive knowledge regarding optical characteristics is essential for determining the optimal utilization of materials in various devices. Cerium oxide exhibits a markedly enhanced optical response compared to alternative materials, attributable to its remarkable absorption associated with pertinent charge transfer mechanisms. In this context, we present a detailed optical investigation for $CeO_2$@PVP, $CeO_2$:Sm@PVP and $CeO_2$:Sm:Li@PVP. The absorption spectra of $CeO_2$, $Sm^{3+}$ doped $CeO_2$ NFs and different (1, 2, 3, 5 and 7) wt.% $Li^+$ doped 0.02$Sm^{3+}$:$CeO_2$ NFs, as determined using UV–visible absorption spectroscopy, are depicted in Fig. 4, which shows that the obtained $E_g$ values are compatible with similar compounds in the literature. Optical properties play a major role in the photodynamic characteristics of the NFs. The optical characteristics of the synthesized NPs were investigated via UV–vis absorption spectroscopy [45,46]. The absorption spectra reveal significant changes in the overall absorption of $CeO_2$ NPs with $Sm^{3+}$ and $Li^+$ doping. To further elaborate on the $Sm^{3+}$ and $Li^+$ doping-induced effects on the optical properties of $CeO_2$ NPs, band gap energies for the synthesized NPs were determined using the Tauc relation as follows [47]:

$$(\alpha h\nu)^{1/n} = A\left(h\nu - E_g\right) \tag{8}$$

Here, α is the optical absorption coefficient, hν is the photon energy, $E_g$ is the direct band gap energy (n = 1/2 for direct transition) and A is a constant. The band gap energies for the synthesized NFs were obtained by extrapolating the linear portion of the energy curve of $(\alpha h\nu)^2$ to the energy axis, as shown in Fig. 4. The calculated band gap energy $E_g$ for undoped $CeO_2$@PVP NF was observed to be 3.63 eV. Table 4 shows the comparison of the band gap with those previously reported. This is in good agreement with the previously reported values. This value of $E_g$ decreases systematically to 3.26 eV with $Sm^{3+}$ doping, while rises systematically to 3.69 eV with $Li^+$ doping, uncovering the significant effects of $Sm^{3+}$ and $Li^+$ ions on the optical properties of $CeO_2$PVP NFs. As a result of doping with $Sm^{3+}$ ions, the narrowing of the $E_g$ energy in $CeO_2$:Sm@PVP NFs compared to $CeO_2$@PVP releases oxygen and triggers the formation of $Ce^{3+}$ from $Ce^{4+}$. This increases the amount of $Ce^{3+}$ states, leading to the formation of localized energy states closer to the conduction band and the narrowing of the band gap. This narrowing of the band gap leads to a reduction in crystallite size, leading to similar changes in microstructural parameters. Surprisingly, co-doping of $Sm^{3+}$ and $Li^+$ in $CeO_2$@PVP NFs caused a small increase in the band gap, which is presumed to be due to the strong interaction of $Li^+$ ions with oxygen defects formed in the crystal lattice, increasing the band gap. This change in the band gap is probably due to the decrease in the oxygen vacancy content. Defects in the $CeO_2$ lattice due to oxygen vacancies can be formed by impurity levels in the local bonds, resulting in the filling of the vacancy by the strong interaction of $Li^+$ ions. This can lead to a decrease in the level of oxygen vacancy defects in the host matrix, an increase in crystallite size and $E_g$ band gap. These findings demonstrate that the obtained data are in good agreement with the XRD analysis as given in Table 1.

El-Habib et al. [48] observed a decrease in the $E_g$ of Gd-doped $CeO_2$ and Nd-doped $CeO_2$ nanostructured thin films. In their report, they suggested that the addition of these doping cations caused a transformation from $Ce^{4+}$ to $Ce^{3+}$ leading to the formation of oxygen vacancies. These vacancies, therefore, act as defects in the cerium oxide band structure by introducing impurity levels between the $O_{2p}$ and $Ce_{4f}$ states. This results in a narrowing of the band gap energy and a reduction in crystallite size. Lee et al. [49] obtained similar behavior for $CeO_2$ and Ho-doped $CeO_2$ NPs. They calculated the $E_g$ energies in the range of 3.35eV for $CeO_2$ and 3.31–3.27eV for $Ho^{3+}$ doped $CeO_2$ NPs. They reported that this narrowing of the band gap may be responsible for the formation of oxygen vacancy defects, and disruptions in local bonds in the $CeO_2$ lattice.

### 3.5. Photoluminescence analysis

PL is a valuable tool to study $e^-$ and $h^+$ photogeneration in a NF and the recombination of these charge carriers during emission. The room temperature PL spectrum of all NFs with near ultraviolet excitation (349 nm) is shown in Fig. 5 and Fig. S2. The PVP polymer matrix was characterized by a broad emission band in the visible region with the emission peak centered at 514 nm (Fig. S2). These emission bands probably indicate n→π* or π→π* electron transition intraligand charge transfer (ILCT) [42,52–54]. As shown in Fig. 5a, the spectra consist of a broad band centered at approximately 400–700 nm with a weak peak at 574 nm. The as-synthesized sample showed a broad emission band centered at 515 nm, and this broad spectrum can probably be attributed to two main reasons: i) The n→π* or π→π* electron transition intraligand charge transfer (ILCT) of the PVP polymer matrix or ii) the transition of the electron from the localized $Ce_{4f}$ state to the valence band of $O_{2p}$. On the other hand, the rather small emission peak at 574 nm could be due to defect states existing between the $Ce_{4f}$ states and the $O_{2p}$ valence band. Moreover, one emission nature has gradually diminished, giving rise to a broad spectrum band [55]. Moreover, Fig. 5b and (c) depicted the PL spectra of $Sm^{3+}$ doped $CeO_2$ NF mats. The emission peaks of $CeO_2$:$Sm^{3+}$ NFs were detected at 574, 615 and 669 nm in the yellow-orange-red region. The emission peaks observed at 574, 615 and 669 nm correspond to $^4G_{5/2} \rightarrow {}^6H_{5/2}$, $^4G_{5/2} \rightarrow {}^6H_{7/2}$ and $^4G_{5/2} \rightarrow {}^6H_{9/2}$ electronic transitions, respectively (Fig. 5b) [56–58]. All transitions are well illustrated in the schematic diagram in Fig. 6. The emission spectra show a transition at 615 nm ($^4G_{5/2} \rightarrow {}^6H_{7/2}$) which is partly magnetic dipole and partly forced electric dipole with orange emission as given by the selection rule $\Delta J = \pm 1$. At 574 nm, a forbidden magnetic dipole transition with dominant intensity corresponding to the $^4G_{5/2} \rightarrow {}^6H_{5/2}$ transition ($\Delta J = 0$, i.e., values of $J \neq 0 \leftrightarrow 0$) is observed and the luminescence is independent of the symmetry of the centers. The magnetic dipole transition $\Delta j = 0$ obeys the ±1 selection rule, where j is the total angular momentum [59]. A hypersensitive peak at 669 nm is also observed, attributed to the electric dipole-allowed transition $^4G_{5/2} \rightarrow {}^6H_{9/2}$ with weak intensity $\Delta J = \pm 2$, which completely obeys the electric dipole transition rule. This transition is symmetry dependent and its intensity decreases with increasing local symmetry. $Sm^{3+}$ can be used as a structural probe to study the symmetry environment of the structure. In general, the intensity of the PL emission peak is due to ED transitions, which are markedly affected by the local environment of the doped ion occupying the luminescent center. However, the intensity of the emission peak may also arise due to MD transitions, which are probably less affected by the crystal field environment. In this context, for the elucidation of the symmetry nature of the local medium, the ratio of the intensity of the ED and MD transitions is a crucial parameter known as the asymmetry ratio. The asymmetry ratio can be evaluated using the following equation:

$$Asymmetry\ ratio(R) = \frac{I_{669nm}}{I_{574nm}} \tag{9}$$

R > 1 indicates that the $Sm^{3+}$ ion occupies a position of asymmetry in the non-inversion center of the local environment. R < 1 indicates that the $Sm^{3+}$ ion occupies a position of high symmetry at the inversion center of the local environment. The asymmetry ratio for the investigated luminescent NF material was determined and presented in Table 3. From the table, it is concluded that the R-value for the phosphor synthesized by varying the $Sm^{3+}$ ion concentration is less than 1. Therefore, the calculated R-value is less than one, indicating that $Sm^{3+}$ ions are located in symmetric regions of the host matrix [60–62].

The photoluminescence intensity of $CeO_2$:$Sm^{3+}$@PVP ($\lambda_{ex}$ = 349 nm) nanofibers increases with $Sm^{3+}$ content, reaching a maximum at a dopant concentration of about x = 0.02 wt%. In contrast, a

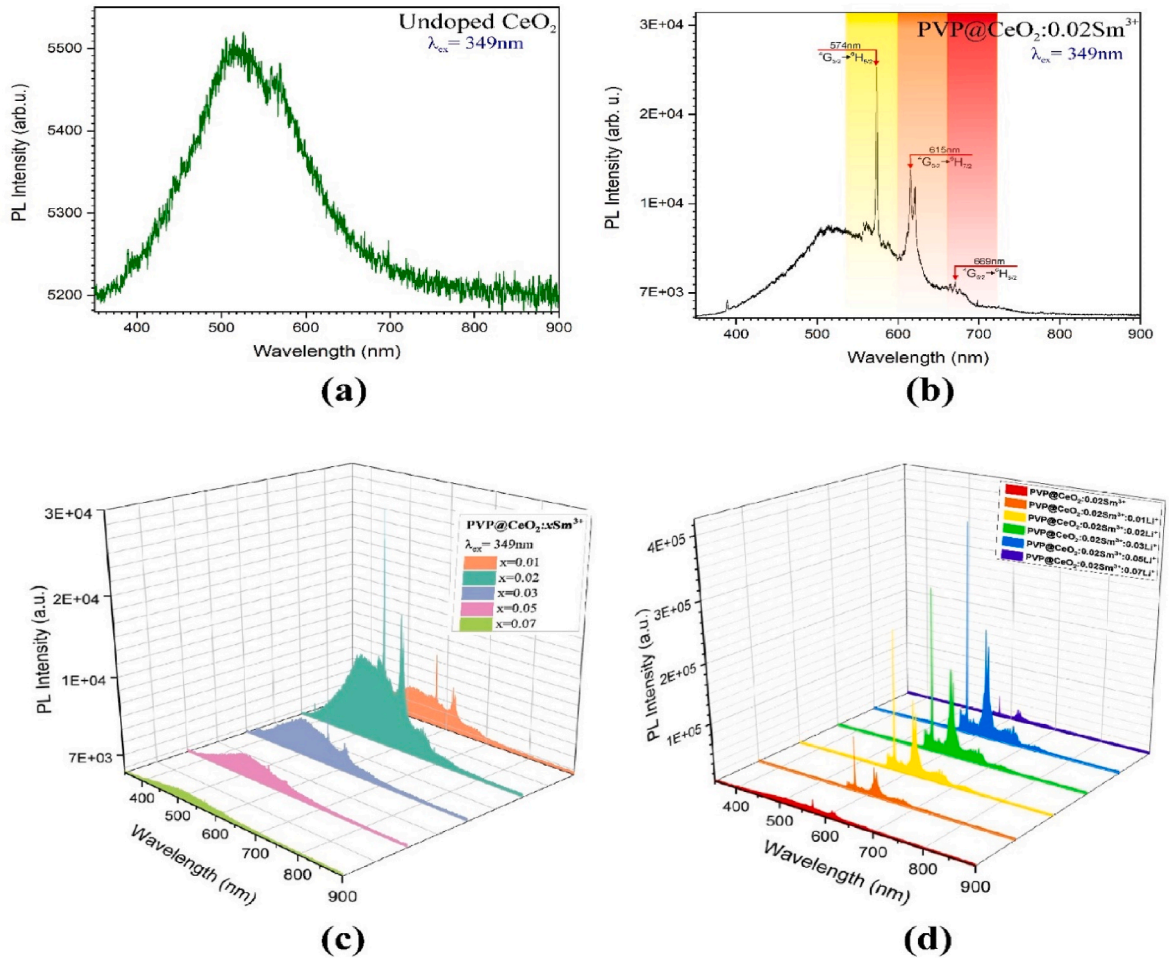


**Fig. 5.** Photoluminescence emission spectra of a) Undoped-$CeO_2$, b) $CeO_2$:0.02$Sm^{3+}$@PVP with possible electronic transition, c) $CeO_2$:x$Sm^{3+}$@PVP (x = 1, 2, 3, 5 and 7 %wt.) and d) $CeO_2$:0.02$Sm^{3+}$:y$Li^{+}$@PVP (y = 1, 2, 3, 5 and 7 %wt.) at room temperature ($\lambda_{ex}$ = 349 nm).

concentration quenching process was observed when more luminescent activator was doped (Fig. 5c). At higher dopant ($Sm^{3+}$) concentrations, a quenching phenomenon occurs, which can be attributed to the reduced distance between $Sm^{3+}$ ions. As the $Sm^{3+}$ ion concentration increases, the distance between neighbouring ions decreases and the interaction between neighbouring $Sm^{3+}$ ions increases. In addition, the proximity of the energy levels of $Sm^{3+}$ dopant ions results in efficient energy transfer from their energy states to the quenching centers. Fig. 5d shows the PL emission spectra of $CeO_2$:0.02$Sm^{3+}$@PVP composite nanofibers with varying $Li^{+}$ co-dopant concentrations under 349 nm excitation. The dominant 574 nm emission peak ($^4G_{5/2} \rightarrow {}^6H_{5/2}$ magnetic dipole transition) intensity increases approximately fourfold as $Li^{+}$ concentration increases from 1 to 5 wt%. This increase is due to $Li^{+}$ ions modifying the local crystal field around $Sm^{3+}$, facilitating efficient radiative recombination. $Li^{+}$ co-doping reduces defects and increases luminescence up to 5 wt%, after which quenching occurs. This quenching is due to energy migration between $Sm^{3+}$ ions and non-radiative recombination in defect sites, which is typical in rare-earth fibers. No significant shift of the emission peak positions is identified at all $Li^{+}$ concentrations, indicating that $Li^{+}$ doping primarily affects the intensity of $Sm^{3+}$ emissions rather than the energy levels involved in the electronic transitions. These results highlight the beneficial effect of $Li^{+}$ co-doping in optimizing the luminescence properties of $CeO_2$:0.02$Sm^{3+}$@PVP phosphors for optoelectronic applications.

Moreover, the presence of non-radiative energy transfer between luminescent centers in host sites significantly reduces the PL intensity. In other words, to understand how energy moves through the host material to understand concentration quenching. This includes radiation reabsorption, energy exchange, and electric multipolar coupling between luminescent centers. Basically, three mechanisms such as radiation reabsorption, exchange interaction and multipolar interaction are responsible for non-radiative energy transfer [63]. The exchange interaction is generally responsible for non-radiative energy transfer if the distance between the nearest neighbouring activator ions is less than 5 Å. Multipolar interaction mediated by non-radiative energy transfer is possible if the distance between the nearest activator ions is greater than 5 Å [64]. In order to further elucidate the type of interaction that triggers the non-radiative energy transfer, the critical distance ($R_c$) between $Sm^{3+}$ ions can be determined using Equation (10) following the Blasse approach [65]:

$$R_c = 2\left(\frac{3V}{4\pi x_c N}\right)^{\frac{1}{3}} \tag{10}$$

Here $x_C$ represents the critical concentration, N represents the number of formula units per unit cell and V represents the unit cell volume. The critical distance of the $Sm^{3+}$ ion-doped $CeO_2$ luminescent material was determined as 19.66 Å. The calculated critical distance ($R_c$ = 19.66 Å) indicates that the non-radiative energy transfer occurs via multipolar interaction. To explain the multipolar interaction phenomenon, Dexter calculated the change in photoluminescence intensity with the multipolar interaction type according to the dopant ion concentration approximation by the following relation [66,67]:

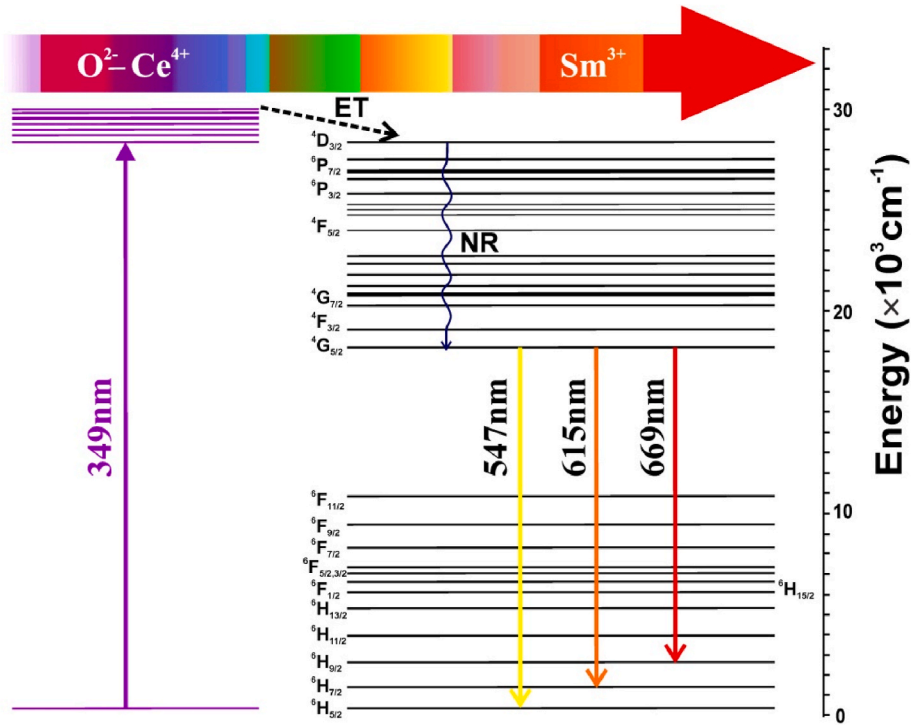


**Fig. 6.** Partial energy level diagram showing the emission of $Sm^{3+}$ ion in $CeO_2$ samples.

**Table 3**
Comparison of asymmetry ratio (R) values depending on $Sm^{3+}$ ion concentration in $CeO_2$@PVP. NFs.

| $Sm^{3+}$ ion concentration | Asymmetry ratio |
|---|---|
| **0.01** | 0.317 |
| **0.02** | 0.911 |
| **0.03** | 0.531 |
| **0.05** | 0.634 |
| **0.07** | 0.810 |

$$\frac{I}{x} = K\left[1 + \beta(x)^{\frac{\theta}{3}}\right]^{-1} \tag{11}$$

where I denotes the intensity of the emission peak, x denotes the dopant ion concentration higher than the critical concentration $x_c$, K and β are constants determined by the host material and experimental setup, and θ is the multipole constant having values of 6, 8, and 10. θ values of 6, 8, and 10 suggest dipole–dipole, dipole–quadrupole and quadrupole–quadrupole type interactions, respectively [68–70]. Fig. 7 shows the plot of log(I/x) versus log(x). From the plot, the slope value is determined as −2.107, which gives the θ value of 6.321, which is approximately close to 6. This value indicates that the dipole-dipole interaction is responsible for the non-radiative energy transfer occurring in the studied luminescent material.

The low-temperature PL spectrum of $Sm^{3+}$-doped $CeO_2$@PVP shown in Fig. 8a and b reveals critical information regarding the luminescent properties of the material under reduced thermal activation. Lower temperatures restrict the phonon-interaction effects, resulting in sharper emission peaks and improved radiative recombination efficiency. This is confirmed by the spectral isometric mapping in Fig. 8a and c, which reveals narrow, well-resolved emission peaks of $Sm^{3+}$ ions. From the observed peaks, the transition from the $^4G_{5/6}$ excited state to the $^6H_{5/2}$ ground state is observed as a plateau-shaped spectral broadband from $CeO_2$ and PVP even at cryogenic temperatures. However, the corresponding transitions from the $^4G_{5/6}$ excited state to the $^6H_{7/2}$ and $^6H_{9/2}$ states are clearly seen. When the low temperature profile of $Li^+$ doped

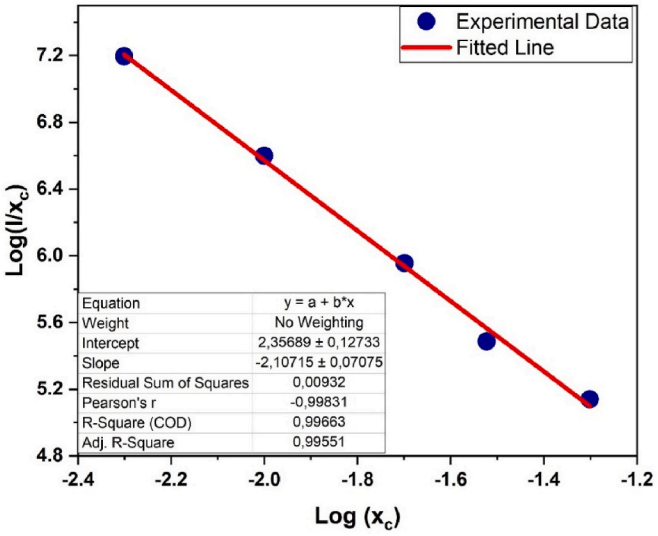


**Fig. 7.** The logarithmic plot of PL intensity at 574 nm (dominant emission peak) versus $Sm^{3+}$ concentration is consistent with a linear trend.

$CeO_2$:0.02$Sm^{3+}$@PVP is examined, the broadband spectral signal disappears and the emission peaks become sharper, and it is clearly seen from the observed peaks that they correspond to the $^6H_j$ (J = 5/2,7,2 and 9/2) manifolds from the $^4G_{5/6}$ excited state. While the $^4G_{5/2} \rightarrow {}^6H_{5/2}$ magnetic dipole transition is dominant in room temperature measurements, the dominant character is the partially magnetic and partially forced electric dipole character attributed to $^4G_{5/2} \rightarrow {}^6H_{7/2}$ as cryogenic temperatures are reached. This dominance has shifted to the transition that characterizes the sharp peaks. This finding shows that the possibility of occupying asymmetric sites in the $CeO_2$ lattice is reduced with $Li^+$ doping and the electric dipole transitions are strengthened by occupying the symmetric lattice sites. Fig. 8c and d shows the temperature-dependent luminescence trends, indicating increasing

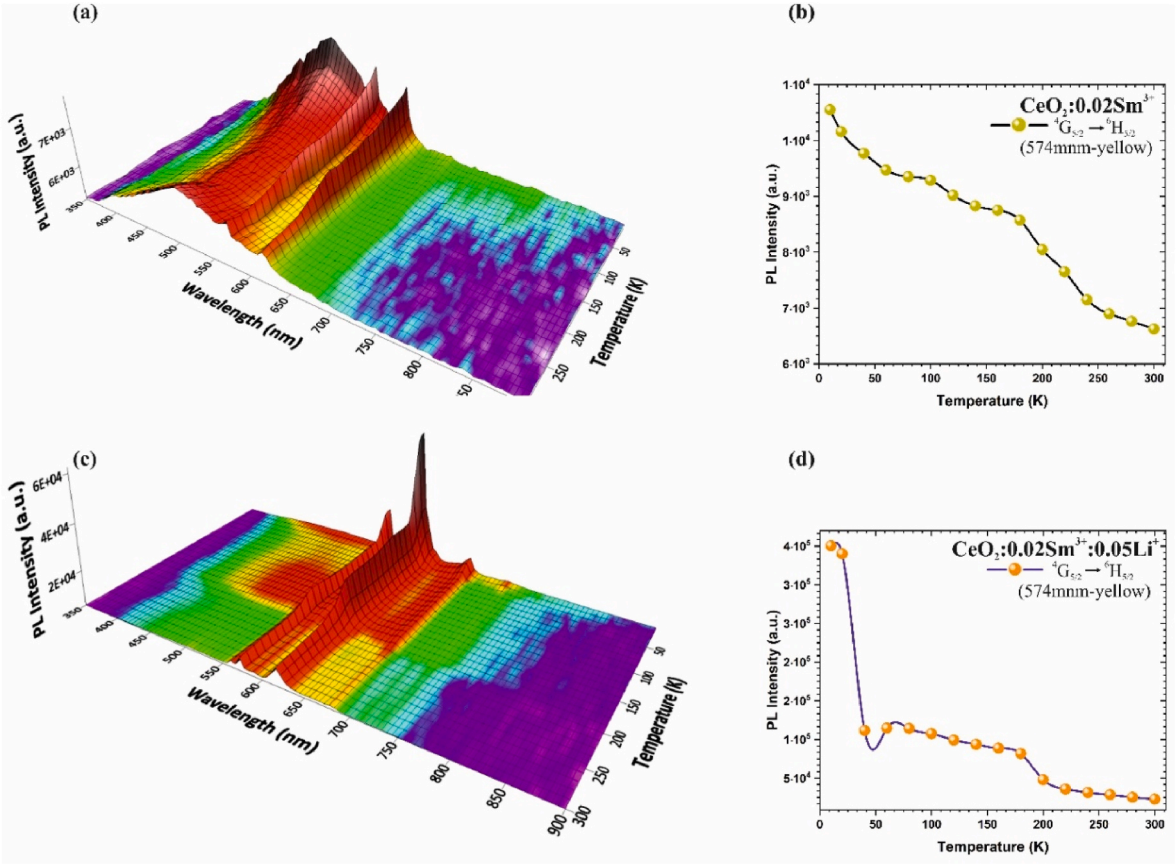


**Fig. 8.** 3D plot of PL intensity as a function of wavelength and temperature for $CeO_2$:0.02$Sm^{3+}$@PVP and $CeO_2$:0.02$Sm^{3+}$,0.05$Li^{+}$@PVP nanofiber, showing significant decrease in intensity from 300 K to 10 K, indicating temperature-dependent quenching mechanisms.

emission as the temperature decreases due to the suppression of non-radiative recombination pathways. Thermal quenching caused by multi-phonon relaxation reduces the emission intensity at higher temperatures. However, cryogenic conditions alleviate this effect, promote radiative decay, and significantly increase the luminescence efficiency, especially at low doping levels. While no shift in peak locations was observed at cryogenic temperatures for $Li^{+}$-doped $CeO_2$:0.02$Sm^{3+}$@PVP composite NFs (Fig. 8c and d), the PL intensity increased by approximately eightfold. This finding suggests that $Li^{+}$ ions promoted efficient radiative recombination by changing the local crystal field around $Sm^{3+}$, and these results can be attributed to the efficient energy transfer between $Li^{+}$ and $Sm^{3+}$ ions.

### 3.6. Colorimetric evaluation

CIE chromaticity coordinates were used to determine the color properties of the emitted light, and colorimetry is a useful method to investigate the true color of the PL of the developed nanofibers. Using the emission spectra excited at 349 nm, the CIE coordinate values for each NF were recorded and are given in Table 4. The values overlap and are quite close to each other. The CIE profile of typical samples $CeO_2$, $CeO_2$:x$Sm^{3+}$ and $CeO_2$:0.02$Sm^{3+}$:y$Li^{+}$ using the CIE 1931 standard is illustrated in Fig. 9. The correlated color temperature (CCT) value of a lighting source is defined by whether it is significantly cool, neutral, or warm. Cool color sources are those with CCT values greater than 3000 K and are frequently used in commercial lighting. Home appliances typically have CCT values below 3000 K and are therefore considered warm. The CCT values of the samples were determined by applying the McCamy formulation [71].

$$CCT = -437n^3 + +3601n^2 + -6861n + 5514.31 \quad (12)$$

**Table 4**
**CIE** coordinates, CCT (Color Correlation Temperature) and CP% (Color Purity) comparisons of composite NFs without additives and doped at various concentrations.

| Composition | CIE chromaticity coordinates | | *CCT value* | CP |
|---|---|---|---|---|
| | x | y | *(K)* | (%) |
| $CeO_2$@PVP | 0.3103 | 0.3315 | *6617* | 9.5 |
| $CeO_2$:0.01$Sm^{3+}$@PVP | 0.3210 | 0.3589 | *5965* | 5.0 |
| $CeO_2$:0.02$Sm^{3+}$@PVP | 0.2988 | 0.3242 | *7373* | 14.3 |
| $CeO_2$:0.03$Sm^{3+}$@PVP | 0.3030 | 0.3231 | *7128* | 12.6 |
| $CeO_2$:0.05$Sm^{3+}$@PVP | 0.3058 | 0.3155 | *7051* | 11.4 |
| $CeO_2$:0.07$Sm^{3+}$@PVP | 0.4220 | 0.3553 | *2821* | 37.3 |
| $CeO_2$:0.02$Sm^{3+}$:0.01$Li^{+}$@PVP | 0.4839 | 0.3776 | *2122* | 63.3 |
| $CeO_2$:0.02$Sm^{3+}$:0.02$Li^{+}$@PVP | 0.4969 | 0.3838 | *2046* | 68.7 |
| $CeO_2$:0.02$Sm^{3+}$:0.03$Li^{+}$@PVP | 0.5063 | 0.3853 | *1977* | 72.7 |
| $CeO_2$:0.02$Sm^{3+}$:0.05$Li^{+}$@PVP | 0.3676 | 0.3339 | *4067* | 14.5 |

where, (x, y) symbolizes the chromaticity coordinates of the synthesized nanofibers and (xe, ye) symbolizes the chromaticity epicenter (0.3320, 0.1858). The calculated CCT values were found in the range of 5965–7373 K for $CeO_2$:x$Sm^{3+}$ and 1977–4067 K for $CeO_2$:0.02$Sm^{3+}$:y$Li^{+}$. The evaluated CCT values indicate that the prepared $Sm^{3+}$ doped nanofibers are considered as a 'cold' candidate with commercially available properties for solid-state applications. Furthermore, the CCT values of $Li^{+}$ ion doped $CeO_2$:0.02$Sm^{3+}$ nanofibers confirm the transition to the 'neutral-hot' region for solid-state applications. In addition, the color purity (CP) of the nanofibers was calculated using the following equation.

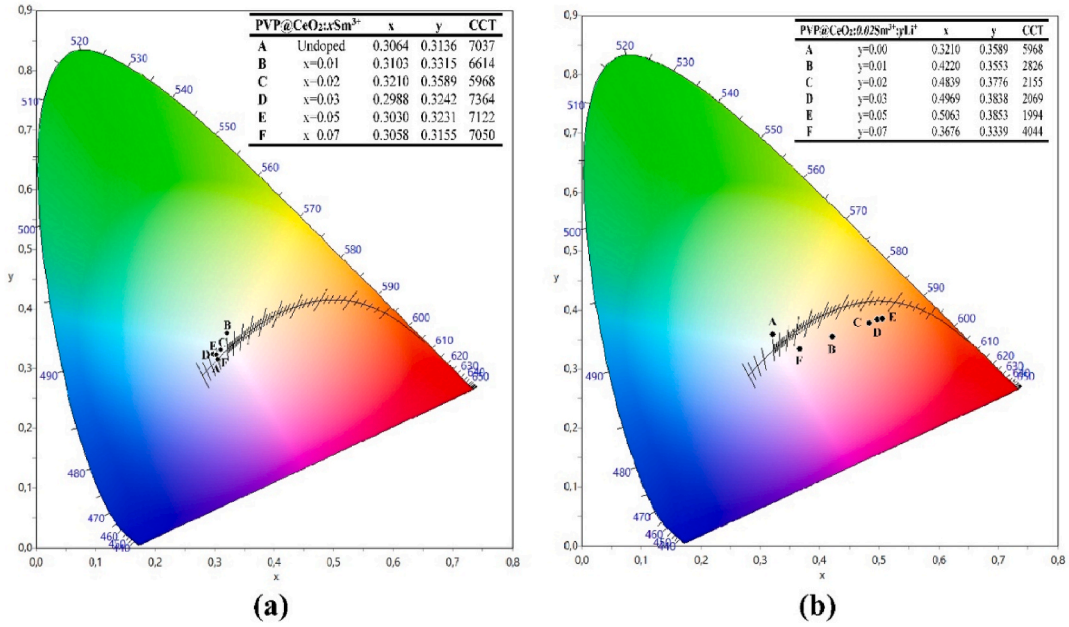


**Fig. 9.** (a) CIE chromaticity coordinates diagram of (a) PVP@$CeO_2$:$xSm^{3+}$ and (b) PVP@$CeO_2$:0.01$Sm^{3+}$,$yLi^{+}$.

$$CP = \frac{\sqrt{(x_s - x_i)^2 + (y_s - y_i)^2}}{\sqrt{(x_d - x_i)^2 + (y_d - y_i)^2}} \times 100\% \quad (13)$$

where, (xs, ys) represent the color coordinates of the NFs, (xi, yi) represent the illuminant spot with color coordinates (0.3101, 0.3162) and (xd, yd) represent the color coordinates of the dominant wavelength. The CP values of the synthesized $CeO_2$, $CeO_2$:$xSm^{3+}$ (1–7 wt%) and $CeO_2$:0.02$Sm^{3+}$:$yLi^{+}$ (1–7 wt%) NFs were calculated and found to be between 9.5 and 72.7 %. CIE chromaticity coordinates, CCT and CP values of the synthesized NFs are given in Table 4.

### 3.7. Antioxidant assay

Antioxidant molecules interact with the DPPH radical through several specific mechanisms to neutralize its free radical activity. One primary mechanism is the Hydrogen Atom Transfer, where a hydrogen atom is directly transferred from the antioxidant to the DPPH radical, effectively neutralizing it [72]. Another mechanism is the Single Electron Transfer, which involves the transfer of a single electron from the antioxidant to the DPPH radical, leading to the formation of a stable radical species. Additionally, Radical Adduct Formation occurs when the antioxidant reacts with the DPPH radical, resulting in a stable adduct [73]. The efficacy of these interactions is also influenced by the binding affinity between the antioxidant and the DPPH radical, which is crucial for effective radical scavenging. Lastly, the stability of the DPPH radical itself can affect these interactions, as factors like solvent and pH play significant roles in its stability [72–74]. Similarly, the interaction of antioxidant molecules with another radical, ABTS, involves several specific mechanisms that neutralize its free radical activity. These mechanisms include hydrogen bonding, electron transfer, and the formation of stable complexes, which collectively contribute to the effective scavenging of the ABTS radical [75,76].

Fig. 10 illustrates the antioxidant efficacy of all examined samples against both ABTS and DPPH radicals. The pure $CeO_2$ sample exhibited the highest radical scavenging activity among all tested samples. Despite

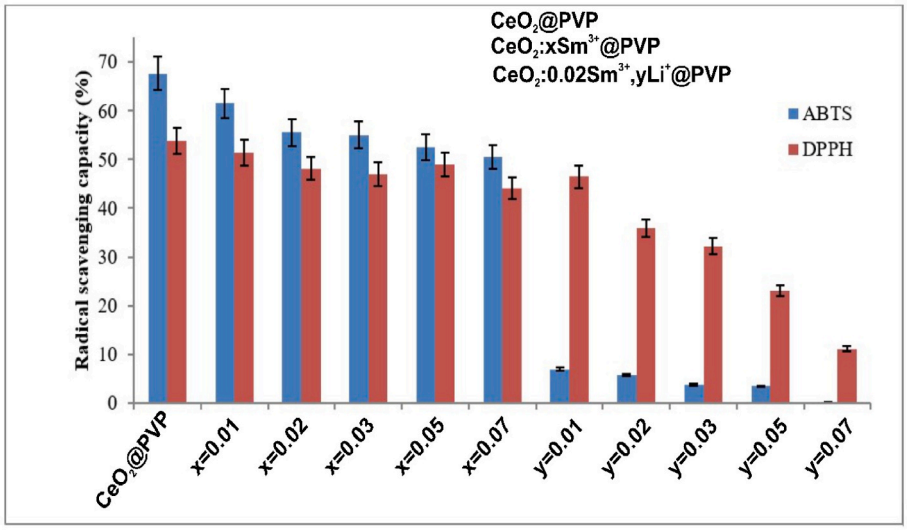


**Fig. 10.** Percent of ABTS and DPPH radicals scavenging activity (antioxidant capacity) of the samples.

significant reductions in the scavenging activity of $CeO_2$:$Sm^{3+}$ samples correlated with increased Sm concentration, both radical scavenging activities remained at or above 50 %. While the DPPH radical scavenging activity of $CeO_2$:$Sm^{3+}$:$Li^+$ samples demonstrated a marked decline with rising Li concentration, the ABTS radical scavenging activity diminished sharply, falling below 10 %. Consequently, the unstable and electron-deficient free radicals are effectively neutralized by $CeO_2$ through mechanisms of hydrogen bonding and electron transfer. Nevertheless, the incorporation of Sm and subsequently $Li^+$ ions into the $CeO_2$ structure hindered the processes of hydrogen bonding and electron transfer, leading to diminished radical scavenging activities.

### 3.8. Biocompatibility of the nanofibers

Biocompatibility and hemocompatibility are critical factors in the development and application of biomaterials, particularly. These properties ensure that materials can interact safely with biological tissues and blood without causing adverse reactions. In other words, biocompatibility refers to a material's ability to perform with an appropriate host response in a specific application, minimizing harmful effects on tissues [77]. The long-term interaction between implanted materials and human tissues is crucial for the success of medical devices, necessitating ongoing evaluation [78]. While biocompatibility and hemocompatibility are paramount for the success of medical materials, challenges remain in balancing innovation with safety. The rapid development of new materials necessitates continuous research and adaptation of testing protocols to ensure safety and material efficacy [79]. Biomaterials have been categorized based on the proportion of hemolysis following interaction with erythrocyte cells; they are deemed highly hemocompatible if the hemolysis rate is below 5 %, hemocompatible within the range of 5–10 %, and non-hemocompatible if exceeding 20 % [80]. According to the data shown in Table 5, all nanofibers exhibited a hemolysis rate of less than 1 %. Consequently, it can be asserted that the samples synthesized in this investigation demonstrate a high degree of hemocompatibility. It is established that PVP, the main component of the nanofibers, is a biocompatible and hemocompatible biodegradable polymer, frequently utilized in various applications such as wound dressings, sutures, and drug delivery systems [81,82]. Moreover, it can be concluded that all other constituents of the nanofibers do not induce any toxicity when integrated with the PVP matrix, thereby promoting cell viability.

### 3.9. Antibacterial activity of the nanofibers

The use of *Escherichia coli* and *Staphylococcus aureus* in evaluating antibacterial activity is primarily due to their clinical significance and varying resistance profiles [83]. *Staphylococcus aureus*, particularly methicillin-resistant strains, poses considerable challenges in clinical environments [84]. *Escherichia coli* is a primary focus of antibacterial research due to its frequent association with various infections and its resistance mechanisms [85]. Therefore, the use of both strains for the investigation of the antibacterial capacity of biomaterials can be considered as a general prediction for their activity. In the present study, the antibacterial efficacy of nanofibers synthesized through the sequential loading of Sm and Li utilizing $CeO_2$@PVP matrices was systematically evaluated. The findings indicated that no antibacterial activity was detected in the complexes generated with $CeO_2$ [86] NPs incorporated into the PVP polymer, which is characterized by its pronounced antibacterial properties against both gram-negative and gram-positive microorganisms. Upon scrutinizing the results depicted in Tables 5 and it was ascertained that the Li-loaded nanofibers exhibited antimicrobial activity against both bacterial strains. Research has documented that the antibacterial properties of biomaterials formulated with Li not only suppress bacterial proliferation [87] but also hinder the development of biofilm layers [88]. It was deduced that the substantial antibacterial activity demonstrated by the nanofibers can be attributed to the incorporation of $Li^+$. Although $Sm^{3+}$ ions are also known to exhibit antibacterial effects due to their unique electronic configuration and their capacity to form stable complexes with various ligands-such as L-aspartic acid, chlorhexidine, and doped $TiO_2$ nanoparticles [89–91] such effects may not always be retained in nanocomposite systems. In certain cases, the antibacterial functionality of $Sm^{3+}$ may diminish or be entirely suppressed, as active ionic species can become chemically bound or immobilized within the polymeric or inorganic matrix [92]. This restricted mobility limits their interaction with bacterial cells, thereby reducing their biological efficacy.

A comparative performance analysis with previously reported $CeO_2$-based systems co-doped with rare-earth and alkali metal ions [93–96] highlights the uniqueness of the present study. While earlier works focused on enhancing crystallinity, modulating oxygen vacancies, and improving luminescence properties—particularly around $Eu^{3+}$ and $Er^{3+}$ ions for optoelectronic applications—this study demonstrates a comprehensive enhancement in $CeO_2$:$Sm^{3+}$:$Li^+$ nanocomposites. Unlike previous reports where the impact of $Li^+$ on $Sm^{3+}$ emission remained ambiguous, the current findings reveal a clear reduction in lattice strain, a nearly tenfold increase in photoluminescence intensity, and a substantial rise in color purity (72.7 %), indicating potential for solid-state lighting (SSL) applications. Additionally, an improvement in antimicrobial performance was observed, further demonstrating the multifunctional potential of the synthesized nanofibers. These results not only confirm the effectiveness of $Li^+$ incorporation but also present new perspectives on the design of multifunctional luminescent biomaterials. The performance dynamics supporting this comparative assessment are summarized in Table 6.

**Table 5**
The ratio of blood hemolysis and the antibacterial efficacy exhibited of the NF samples.

| Nanofibers | % Hemolysis | Inhibition zone (mm) | |
|---|---|---|---|
| | | *S. aureus* | *E. coli* |
| $CeO_2$@PVP | 1.01 ± 0.18 | – | – |
| $CeO_2$:0.01$Sm^{3+}$@PVP | 0.84 ± 0.15 | – | – |
| $CeO_2$:0.02$Sm^{3+}$@PVP | 0.96 ± 0.15 | – | – |
| $CeO_2$:0.03$Sm^{3+}$@PVP | 0.81 ± 0.07 | – | – |
| $CeO_2$:0.05$Sm^{3+}$@PVP | 0.86 ± 0.11 | – | – |
| $CeO_2$:0.07$Sm^{3+}$@PVP | 0.94 ± 0.11 | – | – |
| $CeO_2$:0.07$Sm^{3+}$,0.01$Li^+$@PVP | 0.67 ± 0.01 | 12.7 ± 0.3 | 11.7 ± 1.8 |
| $CeO_2$:0.07$Sm^{3+}$,0.02$Li^+$@PVP | 0.72 ± 0.04 | 11.4 ± 0.2 | 10.3 ± 0.6 |
| $CeO_2$:0.07$Sm^{3+}$,0.03$Li^+$@PVP | 0.91 ± 0.11 | 11.0 ± 0.1 | 10.4 ± 0.6 |
| $CeO_2$:0.07$Sm^{3+}$,0.05$Li^+$@PVP | 0.89 ± 0.20 | 11.3 ± 1.9 | 11.4 ± 0.2 |
| $CeO_2$:0.07$Sm^{3+}$,0.07$Li^+$@PVP | 0.84 ± 0.04 | 11.1 ± 0.9 | 11.0 ± 0.9 |

## 4. Conclusion

In conclusion, $Sm^{3+}$- and $Li^+$-doped $CeO_2$ NPs were synthesized by the co-precipitation method and the synthesized NPs were incorporated into PVP polymer matrix and NFs were successfully obtained by the electrospinning method and their structural, morphological, photoluminescence (PL) and antibacterial properties were systematically analyzed. XRD analysis confirmed that the cubic structure of the $CeO_2$ host underwent small changes in lattice parameters and unit cell volume upon $Sm^{3+}$ doping. Quantitative investigation using the Debye-Scherrer and Williamson-Hall methods underlines that $Sm^{3+}$ doping decreases the crystallite size, while $Sm^{3+}$ and $Li^+$ co-doping increases it, and its effect on changing the lattice strain, which collectively improved the structural and optical properties of the material. PL measurements revealed intense yellow emission at 574 nm ($^4G_{5/2} \rightarrow {}^6H_{5/2}$) instead of the hypersensitive electric dipole transition at 669 nm ($^4G_{5/2} \rightarrow {}^6H_{9/2}$) in $Sm^{3+}$-doped NFs, supporting the magnetic dipole transitions of the $CeO_2$ host, and asymmetric ratio calculations revealed that $Sm^{3+}$ ions occupy a position of high symmetry with the inversion center of the local environment, highlighting the dynamic luminescence mechanisms

**Table 6**
Comparison of the performance dynamics of $CeO_2$ host materials doped with $RE^{3+}$ based on alkali charge compensators.

| Material Composition | Charge Compansators | Performance Dynamics |
|---|---|---|
| $CeO_2$:$Eu^{3+}$ [93] | $Li^+$ | • Higher crystallinity and larger crystallites<br>• Increased crystallinity and decreased oxygen vacancies concentration<br>• The less asymmetry and lower luminescence around $Eu^{3+}$. |
| $CeO_2$:$Sm^{3+}$, $Eu^{3+}$ [94] | $Li^+$ | • The amount of changing oxygen vacancies and $Ce^{3+}$ oxidation states increases defect formation.<br>• The presence of $Li^+$ clearly increases the emission intensity of $Eu^{3+}$, while the increase in the emission intensity of $Sm^{3+}$ is uncertain.<br>• A potential application area for high-efficiency dye-sensitized solar cells. |
| $CeO_2$: $Eu^{3+}$ [95] | $Li^+$ | • Modification of the symmetry around $Eu^{3+}$ sites and improvement of the degree of crystallinity of the host with $Li^+$ co-doping.<br>• Li + ions replace $Ce^{4+}$ sites in the main site instead of interstitial sites.<br>• Significant increase in emission efficiency due to the presence of $Li^+$ ions<br>• Promising orange-red emission efficiency for optoelectronic applications |
| $CeO_2$:$Er^{3+}$ [96] | $Li^+$ | • Improved crystallization and reduced local symmetry with the addition of $Li^+$.<br>• Significant improvement in emission intensity at 1532 nm under 352 nm excitation. |
| $CeO_2$:$Sm^{3+}$ [This work] | $Li^+$ | • Modification of lattice strain.<br>• Notable improvement in PL intensity (~10-fold) with the addition of $Li^+$.<br>• Significant increase in color purity (72.7 %) with the addition of $Li^+$. Potential candidates for SSL applications.<br>• Potential improvement in antimicrobial performance. |

within the $CeO_2$ host. The calculated critical distance ($R_c$ = 19.66 Å) indicated that energy migration occurs predominantly through multipolar interactions facilitated by the structural features of the NF matrix. While room-temperature PL studies appear to exhibit the broad spectrum of the PVP matrix and the $CeO_2$ host, with $Sm^{3+}$ and $Li^+$ co-doping, this effect decreased significantly and the luminescence intensity increased almost ten-fold. When cryogenic temperatures were reached for $CeO_2$:0.02$Sm^{3+}$0.05$Li^+$@PVP NF, the partially magnetic and partially forced electric dipole character attributed to $^4G_{5/2} \rightarrow {}^6H_{7/2}$ became dominant as a result of the $Li^+$ doping decreasing the probability of occupying asymmetric sites in the $CeO_2$ lattice. The analyzed CCT values indicate that the prepared $Sm^{3+}$ doped nanofibers can be considered as "cold" candidates with commercial properties for solid-state applications. Color purity calculations show that $Li^+$ doping results in a significant color purity increase of 72.7 %. The findings provide evidence that $Li^+$ ion doping leads to remarkable improvements in PL properties. While $CeO_2$ and $Sm^{3+}$ ion-doped nanofibers did not exhibit measurable antibacterial activity under the tested conditions, the incorporation of $Li^+$ led to a marked improvement in antimicrobial performance. This suggests that $Li^+$ plays a significant role in enhancing the antibacterial efficacy of the $CeO_2$@PVP nanofiber system. Furthermore, all other components of NFs were observed to cause no toxicity when integrated with the PVP matrix, thus promoting cell viability.

## CRediT authorship contribution statement

**Kubra Nur Kavas:** Visualization, Software, Methodology. **Elif Gungor:** Visualization, Methodology. **Yasemin Acar:** Methodology, Conceptualization. **Fatma Unal:** Visualization, Software, Methodology. **Ozay Eroglu:** Software, Formal analysis. **Mehmet Emin Diken:** Visualization, Software, Methodology. **Serap Dogan:** Methodology, Conceptualization. **Mustafa Burak Coban:** Writing – review & editing, Writing – original draft, Supervision, Software, Project administration, Methodology, Conceptualization.

## Data availability

Data will be made available on request.

## Declaration of competing interest

The authors declare that they have no known competing financial interests or personal relationships that could have appeared to influence the work reported in this paper.

## Acknowledgement

The authors thank to the Research Funds of Balikesir University (Grant No. BAP-2023/198) for the financial support and Balikesir University, Science and Technology Application and Research Center (BUBTAM) for the use of the Photoluminescence Spectrometer.

## Appendix A. Supplementary data

Supplementary data to this article can be found online at https://doi.org/10.1016/j.ceramint.2025.08.192.

## References

[1] N. Baig, I. Kammakakam, W. Falath, Nanomaterials: a review of synthesis methods, properties, recent progress, and challenges, Mater. Adv. 2 (2021) 1821–1871, https://doi.org/10.1039/D0MA00807A.
[2] F. Ruiz-Jorge, J.R. Portela, J. Sánchez-Oneto, E.J. Martínez de la Ossa, Synthesis of Micro- and nanoparticles in Sub- and supercritical water: from the laboratory to larger scales, Appl. Sci. 10 (2020) 5508, https://doi.org/10.3390/app10165508.
[3] D. Mijatovic, J.C.T. Eijkel, A. van den Berg, Technologies for nanofluidic systems: top-down vs. bottom-up—A review, Lab Chip 5 (2005) 492, https://doi.org/10.1039/b416951d.
[4] J. Xue, T. Wu, Y. Dai, Y. Xia, Electrospinning and electrospun nanofibers: methods, materials, and applications, Chem. Rev. 119 (2019) 5298–5415, https://doi.org/10.1021/acs.chemrev.8b00593.
[5] H. Wu, W. Pan, D. Lin, H. Li, Electrospinning of ceramic nanofibers: fabrication, assembly and applications, J. Adv. Ceram. 1 (2012) 2–23, https://doi.org/10.1007/s40145-012-0002-4.
[6] A. Saeed, E. Banoqitah, J.A.M. Abdulwahed, F. Alajmi, A.Y. Madkhli, F.A. Al-Marhaby, K. Albaidani, M. Algethami, A.S. Assran, R. Alwafi, G.M. Asnag, A comprehensive study on structural, optical, electrical, and dielectric properties of PVA-PVP/Ag-$TiO_2$ nanocomposites for dielectric capacitor applications, J. Alloys Compd. 977 (2024) 173412, https://doi.org/10.1016/j.jallcom.2023.173412.
[7] Z.K. Heiba, A.M. El-naggar, M.B. Mohamed, A.M. Kamal, M.M. Osman, A. A. Albassam, G. Lakshminarayana, The effect of concentration of nano CdS/Fe prepared under different conditions on the structural, optical absorption and linear/nonlinear parameters of PVA/PVP polymer blend, Opt. Mater. 122 (2021) 111788, https://doi.org/10.1016/j.optmat.2021.111788.
[8] Z.K. Heiba, A.M. El-naggar, M.B. Mohamed, Y. Altowairqi, A.M. Kamal, Noval properties of PVA/PVP polymer blend doped by nano-ZnO/M (M = Co, Cu, Mn, V), Appl. Phys. A 127 (2021) 976, https://doi.org/10.1007/s00339-021-05129-w.
[9] J. Zhang, H. Liu, Z. Wang, N. Ming, Low-temperature growth of ZnO with controllable shapes and band gaps, J. Cryst. Growth 310 (2008) 2848–2853, https://doi.org/10.1016/j.jcrysgro.2008.02.014.
[10] C.S. Ramya, S. Selvasekarapandian, G. Hirankumar, T. Savitha, P.C. Angelo, Investigation on dielectric relaxations of PVP–NH4SCN polymer electrolyte, J. Non-Cryst. Solids 354 (2008) 1494–1502, https://doi.org/10.1016/j.jnoncrysol.2007.08.038.
[11] T.R. Zhang, R. Lu, X.L. Liu, Y.Y. Zhao, T.J. Li, J.N. Yao, Photochromic polyoxotungstoeuropate $K_{12}[EuP_5W_{30}O_{110}]$/polyvinylpyrrolidone nanocomposite films, J. Solid State Chem. 172 (2003) 458–463, https://doi.org/10.1016/S0022-4596(03)00036-7.
[12] M. Zhou, H. Yang, T. Xian, R.S. Li, H.M. Zhang, X.X. Wang, Sonocatalytic degradation of RhB over $LuFeO_3$ particles under ultrasonic irradiation, J. Hazard. Mater. 289 (2015) 149–157, https://doi.org/10.1016/j.jhazmat.2015.02.054.
[13] D. Channei, B. Inceesungvorn, N. Wetchakun, S. Ukritnukun, A. Nattestad, J. Chen, S. Phanichphant, Photocatalytic degradation of methyl Orange by $CeO_2$ and

Fe–doped $CeO_2$ films under visible light irradiation, Sci. Rep. 4 (2014) 5757, https://doi.org/10.1038/srep05757.
[14] K.X. Lee, B. Hu, P.K. Dubey, M.R. Anisur, S. Belko, A.N. Aphale, P. Singh, High-entropy alloy anode for direct internal steam reforming of methane in SOFC, Int. J. Hydrogen Energy 47 (2022) 38372–38385, https://doi.org/10.1016/j.ijhydene.2022.09.018.
[15] X. Hao, G. Wei, H. Zhang, S. Tan, G. Ji, Defect chemistry-regulated design of doping $CeO_2$ with the enhanced high-temperature low infrared emissivity property, Mater. Today Nano 30 (2025) 100614, https://doi.org/10.1016/j.mtnano.2025.100614.
[16] J.-H. Lee, K.H. Jung, H. Lee, M.K. Son, S.-M. Yun, S.-H. Ahn, K.-R. Lee, S. Lee, D. Kim, S. Hong, S.-S. Hong, HS-133, a novel fluorescent phosphatidylinositol 3-kinase inhibitor as a potential imaging and anticancer agent for targeted therapy, Oncotarget 5 (2014) 10180–10197, https://doi.org/10.18632/oncotarget.2507.
[17] V. Patel, L. Jose, G. Philippot, C. Aymonier, T. Inerbaev, L.R. McCourt, M. G. Ruppert, D. Qi, W. Li, J. Qu, R. Zheng, J. Cairney, J. Yi, A. Vinu, A.S. Karakoti, Fluoride-assisted detection of glutathione by surface $Ce^{3+}/Ce^{4+}$ engineered nanoceria, J. Mater. Chem. B 10 (2022) 9855–9868, https://doi.org/10.1039/D2TB01135B.
[18] F. Meng, Z. Fan, C. Zhang, Y. Hu, T. Guan, A. Li, Morphology-controlled synthesis of $CeO_2$ microstructures and their room temperature ferromagnetism, J. Mater. Sci. Technol. 33 (2017) 444–451, https://doi.org/10.1016/j.jmst.2016.06.018.
[19] L. Wang, Y. Li, J. Liu, Z. Tian, Y. Jing, Regulation of oxygen vacancies in cobalt-cerium oxide catalyst for boosting decontamination of VOCs by catalytic oxidation, Sep. Purif. Technol. 277 (2021) 119505, https://doi.org/10.1016/j.seppur.2021.119505.
[20] J. Shi, H. Li, A. Genest, W. Zhao, P. Qi, T. Wang, G. Rupprechter, High-performance water gas shift induced by asymmetric oxygen vacancies: gold clusters supported by ceria-praseodymia mixed oxides, Appl. Catal. B Environ. 301 (2022) 120789, https://doi.org/10.1016/j.apcatb.2021.120789.
[21] R.K. Singhal, P. Kumari, A. Samariya, S. Kumar, S.C. Sharma, Y.T. Xing, E. B. Saitovitch, Role of electronic structure and oxygen defects in driving ferromagnetism in nondoped bulk $CeO_2$, Appl. Phys. Lett. 97 (2010), https://doi.org/10.1063/1.3507290.
[22] R.K. Singhal, S. Kumar, A. Samariya, M. Dhawan, S.C. Sharma, Y.T. Xing, Investigating the mechanism of ferromagnetic exchange interaction in non-doped $CeO_2$ with regard to defects and electronic structure, Mater. Chem. Phys. 132 (2012) 534–539, https://doi.org/10.1016/j.matchemphys.2011.11.066.
[23] I. Hussain, G. Tanimu, S. Ahmed, C.U. Aniz, H. Alasiri, K. Alhooshani, A review of the indispensable role of oxygen vacancies for enhanced $CO_2$ methanation activity over $CeO_2$-based catalysts: uncovering, influencing, and tuning strategies, Int. J. Hydrogen Energy 48 (2023) 24663–24696, https://doi.org/10.1016/j.ijhydene.2022.08.086.
[24] U.J. Etim, C. Zhang, Z. Zhong, Impacts of the catalyst structures on $CO_2$ activation on catalyst surfaces, Nanomaterials 11 (2021) 3265, https://doi.org/10.3390/nano11123265.
[25] V.R. Mala, A. Princy, K.J. Albert, S.M. Moses Kennedy, Enhancement of green light emission from the $LiSrVO_4:Tb^{3+}$ doped vanadate phosphor by charge compensation via co-doping of the alkali metal ions ($Li^+/Na^+/K^+$), J. Lumin. 263 (2023) 119948, https://doi.org/10.1016/j.jlumin.2023.119948.
[26] Q. Zeng, W. He, N. Zhang, D. Guo, Insight into luminescence properties of $Li^+$ co-doped $Sr_2SnO_4:Eu^{3+}$ phosphors by co-precipitation assisted hydrothermal synthesis, J. Lumin. 253 (2023) 119452, https://doi.org/10.1016/j.jlumin.2022.119452.
[27] V. Chauhan, P. Deshmukh, S. Satapathy, P.C. Pandey, Greenish-yellow emission from rare-earth free $Li^+$ doped zinc vanadate phosphor, Results Phys. 39 (2022) 105689, https://doi.org/10.1016/j.rinp.2022.105689.
[28] Y. Guo, D. Wang, F. Wang, Effect of $Li^+$ ions doping on microstructure and upconversion luminescence of $CeO_2:Er^{3+}$ translucent ceramics, Opt. Mater. 42 (2015) 390–393, https://doi.org/10.1016/j.optmat.2015.01.033.
[29] K.Y. Jung, J.C. Lee, D.S. Kim, B.-K. Choi, W.-J. Kang, Co-doping effect of monovalent alkali metals on optical properties of $CeO_2$:Eu nanophosphor prepared by spray pyrolysis and application for preparing pearlescent pigments with red emission, J. Lumin. 192 (2017) 1313–1321, https://doi.org/10.1016/j.jlumin.2017.09.017.
[30] A.S. Altowyan, U.H. Kaynar, H. Aydin, M.B. Coban, Z.G. Portakal, S. Akça-Özalp, J. Hakami, M. Ayvacikli, M. Topaksu, N. Can, Enhanced photoluminescence properties of $Eu^{3+}/Li^+$ co-doped $ZrO_2$: a focus on red and far-red emissions, J. Photochem. Photobiol. Chem. 466 (2025) 116408, https://doi.org/10.1016/j.jphotochem.2025.116408.
[31] M.E. Diken, B. Koçer Kizilduman, S. Doğan, M. Doğan, Antibacterial and antioxidant phenolic compounds loaded PCL biocomposites for active food packaging application, J. Appl. Polym. Sci. 139 (2022), https://doi.org/10.1002/app.52423.
[32] Y. Liu, D. Cai, J. Yang, Y. Wang, X. Zhang, S. Yin, In vitro hemocompatibility evaluation of poly (4-hydroxybutyrate) scaffold, Int. J. Clin. Exp. Med. 7 (2014) 1233–1243. http://www.ncbi.nlm.nih.gov/pubmed/24995078.
[33] F. Ünal, Straightforward route for terbium oxide powders: synthesis, morphology, and microstructural parameters, Int. J. Mater. Res. 113 (2022) 287–294, https://doi.org/10.1515/ijmr-2021-8484.
[34] E. Emil, S. Gürmen, Estimation of yttrium oxide microstructural parameters using the Williamson–Hall analysis, Mater. Sci. Technol. 34 (2018) 1549–1557, https://doi.org/10.1080/02670836.2018.1490857.
[35] V. Saraswathi A, P. H M, K. R, A. Princy, S.M.M. Kennedy, M.I. Sayyed, T. A. Hanafy, S.D. Kamath, Synthesis and exploration of intricate optical and thermal attributes of $Sm^{3+}$ doped novel borate phosphors, Ceram. Int. (2025), https://doi.org/10.1016/j.ceramint.2025.02.081.
[36] A.S. Altowyan, U.H. Kaynar, C. Gök, H. Aydin, J. Hakami, M.B. Coban, A. Canimoglu, N. Can, Photoluminescence characteristics and Judd–Ofelt analysis of $YBa_3(BO_3)_3:Tb^{3+}$ phosphors co-doped with $Li^+$, $Na^+$, and $K^+$, J. Lumin. 286 (2025) 121380 https://doi.org/10.1016/j.jlumin.2025.121380.
[37] M.R. Khaleel, F.S. Hashim, A.H.O. Alkhayatt, Preparation, characterization, and the antimicrobial activity of PVA-PVP/ZnO nanofiber films via indigenous electrospinning setup, J. Mol. Struct. 1310 (2024) 138325, https://doi.org/10.1016/j.molstruc.2024.138325.
[38] V. Rahmanian, T. Pirzada, E. Barbieri, S. Iftikhar, F. Li, S.A. Khan, Mechanically robust, thermally insulating and photo-responsive aerogels designed from sol-gel electrospun PVP-$TiO_2$ nanofibers, Appl. Mater. Today 32 (2023) 101784, https://doi.org/10.1016/j.apmt.2023.101784.
[39] Y. Liu, Y. Liu, X. Li, Y. Qian, L. Lv, Y. Wang, Fabrication and research of $Mg(OH)_2$/PCL/PVP nanofiber membranes loaded by antibacterial and biosafe Mg(OH)2 nanoparticles, Polym. Test. 112 (2022) 107635, https://doi.org/10.1016/j.polymertesting.2022.107635.
[40] K. Kumar, E. Selvarajan, P. Balasubramanian, Preparation and studies of cerium dioxide ($CeO_2$) nanoparticles by microwave-assisted solution method, Recent res, Sci. Technol. 2 (2010) 37–41.
[41] B. Ghorani, N. Tucker, Fundamentals of electrospinning as a novel delivery vehicle for bioactive compounds in food nanotechnology, Food Hydrocoll. 51 (2015) 227–240, https://doi.org/10.1016/j.foodhyd.2015.05.024.
[42] M.B. Coban, E. Gungor, Y. Acar, F.K. Alpaslan, H.K. Subasat, Multifunctional Dy@PVP and Ho@PVP one-dimensional nanofibers: electrospinning synthesis, luminescent and magnetic properties, J. Mol. Struct. 1272 (2023) 134117, https://doi.org/10.1016/j.molstruc.2022.134117.
[43] H. Kara, G. Oylumluoglu, M.B. Coban, Photoluminescence properties of a new Sm (III) Complex/PMMA electrospun composite fibers, J. Cluster Sci. 31 (2020) 701–708, https://doi.org/10.1007/s10876-019-01677-7.
[44] X. Chen, Z. Xue, K. Niu, X. Liu, Wei lv, B. Zhang, Z. Li, H. Zeng, Y. Ren, Y. Wu, Y. Zhang, Li–fluorine codoped electrospun carbon nanofibers for enhanced hydrogen storage, RSC Adv. 11 (2021) 4053–4061, https://doi.org/10.1039/D0RA06500E.
[45] F. Abbas, T. Jan, J. Iqbal, I. Ahmad, M.S.H. Naqvi, M. Malik, Facile synthesis of ferromagnetic Ni doped $CeO_2$ nanoparticles with enhanced anticancer activity, Appl. Surf. Sci. 357 (2015) 931–936, https://doi.org/10.1016/j.apsusc.2015.08.229.
[46] H.S. Batool, M.J.I. Khan, I. Taj, J. Ahmad, M. Yousaf, M. Yousaf, DFT investigations of structural, electronic, magnetic, and optical properties of $CeO_{2-X}$ (X=Mo/Cr) and Mo-Cr co-doped $CeO_2$ for optoelectronic applications, Solid State Commun. 385 (2024) 115499, https://doi.org/10.1016/j.ssc.2024.115499.
[47] P.R. Jubu, O.S. Obaseki, A. Nathan-Abutu, F.K. Yam, Y. Yusof, M.B. Ochang, Dispensability of the conventional Tauc's plot for accurate bandgap determination from UV–vis optical diffuse reflectance data, Res. Opt. 9 (2022) 100273, https://doi.org/10.1016/j.rio.2022.100273.
[48] A. El-Habib, B. Brioual, J. Zimou, Z. Rossi, A. Marjaoui, M. Zanouni, A. Aouni, M. Jbilou, M. Diani, M. Addou, Comparative studies on the structural, optical and electrochemical properties of Gd, Nd and In-doped $CeO_2$ nanostructured thin films, Mater. Sci. Semicond. Process. 176 (2024) 108287, https://doi.org/10.1016/j.mssp.2024.108287.
[49] N.S. Leel, M. Kiran, P.A. Alvi, B. Dalela, S. Kumar, S. Dalela, Oxygen vacancies mediated changes in ferromagnetic, optical, photoluminescent and electronic structure properties of Ho-doped $CeO_2$ nanoparticles, Ceram. Int. 50 (2024) 8448–8462, https://doi.org/10.1016/j.ceramint.2023.12.180.
[50] C. Kumaran, I. Baskaran, B. Sathyaseelan, K. Senthilnathan, E. Manikandan, S. Sambasivam, Effect of doping of iron on structural, optical and magnetic properties of $CeO_2$ nanoparticles, Chem. Phys. Lett. 808 (2022) 140110, https://doi.org/10.1016/j.cplett.2022.140110.
[51] G.H. Nagaveni, B. Maheshkumar, S.V. Halse, M.N. Kalasad, Optical and electrical properties of amine functionalized $CeO_2$ nanoparticles, Chem. Phys. Impact 8 (2024) 100522, https://doi.org/10.1016/j.chphi.2024.100522.
[52] A. Donmez, M.B. Coban, C. Kocak, G. Oylumluoglu, U. Baisch, H. Kara, Synthesis, characterization and photoluminescence studies of new Cu(II) complex, Mol. Cryst. Liq. Cryst. 652 (2017) 213–222, https://doi.org/10.1080/15421406.2017.1358013.
[53] M.B. Coban, Hydrothermal synthesis, crystal structure, luminescent and magnetic properties of a new mononuclear $Gd^{III}$ coordination complex, J. Mol. Struct. 1162 (2018) 109–116, https://doi.org/10.1016/j.molstruc.2018.02.089.
[54] U. Erkarslan, A. Donmez, H. Kara, M. Aygun, M.B. Coban, Synthesis, structure and photoluminescence performance of a new $Er^{3+}$-Cluster-Based 2D coordination polymer, J. Cluster Sci. 29 (2018) 1177–1183, https://doi.org/10.1007/s10876-018-1434-y.
[55] A. Balamurugan, M. Sudha, S. Surendhiran, R. Anandarasu, S. Ravikumar, Y. A. Syed Khadar, Hydrothermal synthesis of samarium (Sm) doped cerium oxide ($CeO_2$) nanoparticles: characterization and antibacterial activity, Mater. Today Proc. 26 (2020) 3588–3594, https://doi.org/10.1016/j.matpr.2019.08.217.
[56] M. Balestrieri, S. Colis, M. Gallart, G. Schmerber, M. Ziegler, P. Gilliot, A. Dinia, Photoluminescence properties of rare earth (Nd, Yb, Sm, pr)-doped $CeO_2$ pellets prepared by solid-state reaction, J. Mater. Chem. C 3 (2015) 7014–7021, https://doi.org/10.1039/C5TC00075K.
[57] I. Mechergui, H. Fares, S.A. Mohamed, M. Nalin, H. Elhouichet, Coupling between surface plasmon resonance and $Sm^{3+}$ ions induced enhancement of luminescence properties in fluoro-tellurite glasses, J. Lumin. 190 (2017) 518–524, https://doi.org/10.1016/j.jlumin.2017.06.013.

[58] J. Zhang, C. Chen, X. Zhang, X. Wang, W. Shi, B. Han, Photoluminescence properties of Sm3+ doped barium borophosphate phosphors, Optik 158 (2018) 1499–1503, https://doi.org/10.1016/j.ijleo.2018.01.048.

[59] G. Blasse, B.C. Grabmaier, Luminescent Materials, Springer Berlin Heidelberg, Berlin, Heidelberg, 1994, https://doi.org/10.1007/978-3-642-79017-1.

[60] C.P. Reddy, V. Naresh, B.C. Babu, S. Buddhudu, Photoluminescence and energy transfer process in $Bi^{3+}$/$Sm^{3+}$ Co-Doped phosphate zinc lithium glasses, Adv. Mater. Phys. Chem. 4 (2014) 165–171, https://doi.org/10.4236/ampc.2014.49019.

[61] S. Chahar, V.B. Taxak, M. Dalal, S. Singh, S.P. Khatkar, Structural and photoluminescence investigations of $Sm^{3+}$ doped $BaY_2ZnO_5$ nanophosphors, Mater. Res. Bull. 77 (2016) 91–100, https://doi.org/10.1016/j.materresbull.2016.01.027.

[62] C. Liang, X. Huang, W. Huang, Relationship of the different Ca sites in the matrix with luminescence properties of orange–red emitting $Li_{0.04}Ca_{0.96-x}SiO_3:Sm_x$ phosphors, Ceram. Int. 48 (2022) 13719–13731, https://doi.org/10.1016/j.ceramint.2022.01.253.

[63] S. Limbu, L.R. Singh, Exploring luminescent color tunability and efficient energy transfer mechanism of a single-phased hexagonal nanophosphor for white light emitting diodes (WLEDs) application, J. Alloys Compd. 970 (2024) 172580, https://doi.org/10.1016/j.jallcom.2023.172580.

[64] B. Lei, S.-Q. Man, Y. Liu, S. Yue, Luminescence properties of $Sm^{3+}$-doped $Sr_3Sn_2O_7$ phosphor, Mater. Chem. Phys. 124 (2010) 912–915, https://doi.org/10.1016/j.matchemphys.2010.08.032.

[65] G. Blasse, Energy transfer in oxidic phosphors, Phys. Lett. 28 (1968) 444–445, https://doi.org/10.1016/0375-9601(68)90486-6.

[66] D.L. Dexter, A theory of sensitized luminescence in solids, J. Chem. Phys. 21 (1953) 836–850, https://doi.org/10.1063/1.1699044.

[67] D.L. Dexter, J.H. Schulman, Theory of concentration quenching in inorganic phosphors, J. Chem. Phys. 22 (1954) 1063–1070, https://doi.org/10.1063/1.1740265.

[68] A.S. Altowyan, M.B. Coban, U.H. Kaynar, J. Hakami, M. Ayvacikli, A. Hiziroglu, N. Can, Temperature-dependent photoluminescence of novel $Eu^{3+}$, $Tb^{3+}$, and $Dy^{3+}$ doped $LaCa_4O(BO_3)_3$: insights at low and room temperatures, Appl. Radiat. Isot. 208 (2024) 111308, https://doi.org/10.1016/j.apradiso.2024.111308.

[69] G. Souadi, U.H. Kaynar, M. Ayvacikli, M.B. Coban, M. Oglakci, A. Canimoglu, N. Can, Synthesis and photoluminescence characteristics of a novel Eu and Tb doped $Li_2MoO_4$ phosphor, Appl. Radiat. Isot. 175 (2021) 109820, https://doi.org/10.1016/j.apradiso.2021.109820.

[70] A.S. Altowyan, M.B. Coban, U.H. Kaynar, E.A. Çin, M. Ayvacikli, J. Hakami, N. Can, Structural and photoluminescent analysis of novel $Eu^{3+}$ and $Dy^{3+}$ Co-doped ZnO nanoparticles by incorporation of $Li^+$ and $K^+$ ions, Ceram. Int. 50 (2024) 14529–14541, https://doi.org/10.1016/j.ceramint.2024.01.366.

[71] C.S. McCamy, Correlated color temperature as an explicit function of chromaticity coordinates, Color Res. Appl. 17 (1992) 142–144, https://doi.org/10.1002/col.5080170211.

[72] S. Marano, C. Minnelli, L. Ripani, M. Marcaccio, E. Laudadio, G. Mobbili, A. Amici, T. Armeni, P. Stipa, Insights into the antioxidant mechanism of newly synthesized benzoxazinic nitrones: in vitro and in Silico studies with DPPH model radical, Antioxidants 10 (2021) 1224, https://doi.org/10.3390/antiox10081224.

[73] Z. Markovic, Study of the mechanisms of antioxidative action of different antioxidants, J. Serbian Soc. Comput. Mech. 10 (2016) 135–150, https://doi.org/10.5937/jsscm1601135M.

[74] D.I. Tsimogiannis, V. Oreopoulou, The contribution of flavonoid C-ring on the DPPH free radical scavenging efficiency. A kinetic approach for the 3′,4′-hydroxy substituted members, Innov. Food Sci. Emerg. Technol. 7 (2006) 140–146, https://doi.org/10.1016/j.ifset.2005.09.001.

[75] X. Wang, B. Chen, K.S. Bhullar, H. Yang, X. Luo, J. Fu, H. Liu, D. Su, D. Sun, Y. Qiao, W. Zhou, Investigation of antioxidant mechanisms of novel peptides derived from Asian swamp eel hydrolysate in chemical systems and AAPH-induced human erythrocytes, Antioxidants 13 (2024) 888, https://doi.org/10.3390/antiox13080888.

[76] M. Gorbachev, N. Gorinchoy, I. Balan, Some particularities of the reaction between antioxidant phenolic acids and the free radical ABTS•+: a comparative DFT study for the gas phase and ethanol, Chem. J. Mold. 17 (2022) 24–30, https://doi.org/10.19261/cjm.2021.919.

[77] M. Mozafari, Principles of biocompatibility, in: Handb. Biomater. Biocompat., Elsevier, 2020, pp. 3–9, https://doi.org/10.1016/B978-0-08-102967-1.00001-3.

[78] B.A. Fiedler, Role of biocompatibility, in: Manag. Med. Devices Within a Regul. Framew., Elsevier, 2017, pp. 91–108, https://doi.org/10.1016/B978-0-12-804179-6.00006-X.

[79] S.E. Gad, S.C. Gad, Biocompatibility, in: Encycl. Toxicol., Elsevier, 2024, pp. 91–98, https://doi.org/10.1016/B978-0-12-824315-2.01099-X.

[80] B. Yilmaz, S. Doğan, S. Çelikler Kasimoğullari, Hemocompatibility, cytotoxicity, and genotoxicity of poly(methylmethacrylate)/nanohydroxyapatite nanocomposites synthesized by melt blending method, Int. J. Polym. Mater. Polym. Biomater. 67 (2018) 351–360, https://doi.org/10.1080/00914037.2017.1331349.

[81] S.M.H. Gillani, A. Mughal, R.A.A. Khan, M.H. Nawaz, Z. Razzaq, M.S. Ismat, R. Hussain, A. Wadood, S. Ahmed, B. Minhas, M. Abbas, T. Vayalpurayil, M.A. U. Rehman, Development of hybrid polyvinylpyrrolidone/carboxymethyl cellulose/collagen incorporated oregano scaffolds via direct ink write printing for potential wound healing applications, Int. J. Biol. Macromol. 278 (2024) 134528, https://doi.org/10.1016/j.ijbiomac.2024.134528.

[82] M. Kurakula, G.S.N. Koteswara Rao, Moving polyvinyl pyrrolidone electrospun nanofibers and bioprinted scaffolds toward multidisciplinary biomedical applications, Eur. Polym. J. 136 (2020) 109919, https://doi.org/10.1016/j.eurpolymj.2020.109919.

[83] G. Liu, P. Qin, X. Cheng, L. Wu, W. Zhao, W. Gao, Evaluation of the mechanistic basis for the antibacterial activity of ursolic acid against Staphylococcus aureus, Front. Microbiol. 15 (2024), https://doi.org/10.3389/fmicb.2024.1389242.

[84] M. Rahmani, B. Astani, A. Jaliani, H. Kheirandish, Evaluation of kinetic stability and anti-staphylococcal activity of recombinant LasA protein produced in Escherichia coli, Iran, J. Basic Med. Sci. 24 (2021) 851–855, https://doi.org/10.22038/ijbms.2021.54563.12250.

[85] H. Frickmann, A. Hahn, S. Berlec, J. Ulrich, M. Jansson, N.G. Schwarz, P. Warnke, A. Podbielski, On the etiological relevance of Escherichia coli and Staphylococcus aureus in superficial and deep infections – a hypothesis-forming, retrospective assessment, Eur. J. Microbiol. Immunol. 9 (2019) 124–130, https://doi.org/10.1556/1886.2019.00021.

[86] O.L. Pop, A. Mesaros, D.C. Vodnar, R. Suharoschi, F. Tăbăran, L. Mageruşan, I. S. Tódor, Z. Diaconeasa, A. Balint, L. Ciontea, C. Socaciu, Cerium oxide nanoparticles and their efficient antibacterial application in vitro against gram-positive and gram-negative pathogens, Nanomaterials 10 (2020) 1614, https://doi.org/10.3390/nano10081614.

[87] H. Bareke, A.A. Oladipo, Antimicrobial activity of biogenic-synthesized novel bimetallic nanospinel LiCu-ferrite particles: experimental and computational studies, J. Mol. Struct. 1296 (2024) 136823, https://doi.org/10.1016/j.molstruc.2023.136823.

[88] M. Zehra, Y. Usmani, J. Shafiq, A. Khan, M. Zafar, M. Raza Mirza, S.R. Shah, A. Al-Harrasi, S.M. Hasan, A. Farooqui, A. Ahmed, In vitro and in vivo antimicrobial potential of lithium complex against multi-drug resistant Acinetobacter baumannii, Microbiol. Spectr. 11 (2023), https://doi.org/10.1128/spectrum.01930-23.

[89] Y. Hui, H. Qizhuang, Y. Jing, Z. Wenjie, Synthesis, characterization and antibacterial properties of rare Earth ($Ce^{3+}$, $Pr^{3+}$, $Nd^{3+}$, $Sm^{3+}$, $Er^{3+}$) complexes with L-Aspartic acid and o-Phenanthroline, J. Rare Earths 24 (2006) 4–8, https://doi.org/10.1016/S1002-0721(07)60309-3.

[90] M. Calinescu, C. Stoica, M. Nita-Lazar, Complex compounds of Sm(III) with chlorhexidine synthesis, characterization, luminescent properties and antibacterial activity, Rev. Chim. 70 (2019) 6–12, https://doi.org/10.37358/RC.19.1.6840.

[91] Y. Cao, Z. Zhao, J. Yi, C. Ma, D. Zhou, R. Wang, C. Li, J. Qiu, Luminescence properties of $Sm^{3+}$-doped TiO2 nanoparticles: synthesis, characterization, and mechanism, J. Alloys Compd. 554 (2013) 12–20, https://doi.org/10.1016/j.jallcom.2012.11.149.

[92] S.L. Iconaru, A. Groza, S. Gaiaschi, K. Rokosz, S. Raaen, S.C. Ciobanu, P. Chapon, D. Predoi, Antimicrobial properties of samarium doped hydroxyapatite suspensions and coatings, Coatings 10 (2020) 1124, https://doi.org/10.3390/coatings10111124.

[93] W. Huang, Y. Tan, D. Li, H. Du, X. Hu, G. Li, Y. Kuang, M. Li, D. Guo, Improved photo-luminescence by co-doped lithium in the phosphor system $CeO^2$:$Eu^{3+}$, J. Lumin. 206 (2019) 432–439, https://doi.org/10.1016/j.jlumin.2018.10.072.

[94] Y. Tan, Y. Yan, H. Du, X. Hu, G. Li, Y. Kuang, M. Li, D. Guo, Enhanced luminescence via $Li^+$ doping from a $Sm^{3+}$/$Eu^{3+}$ Co-doped cerium oxide phosphor, Opt. Mater. 85 (2018) 538–544, https://doi.org/10.1016/j.optmat.2018.09.012.

[95] N. Van Hai, H.N. Van, Judd–Ofelt intensity parameters and optical properties of Eu/Li co-doped $CeO_2$ phosphor, ChemistrySelect 9 (2024), https://doi.org/10.1002/slct.202400839.

[96] Y. Yang, Y. Cong, D.P. Dong, Y. Xiao, J.Y. Shang, Y. Tong, H.M. Zhang, M. He, J. H. Zhang, Structural and excitation dependent emission properties of octahedral $CeO_2$:$Er^{3+}$ nanocrystal, J. Lumin. 213 (2019) 427–432, https://doi.org/10.1016/j.jlumin.2019.05.009.